Argon behaviour in an inverted Barrovian sequence, Sikkim Himalaya: the consequences of temperature and timescale on $^{40}Ar/^{39}Ar$ mica geochronology

Journal Item

Lithos 238 (2015) 37–51

Contents lists available at ScienceDirect

Lithos

journal homepage: www.elsevier.com/locate/lithos

Argon behaviour in an inverted Barrovian sequence, Sikkim Himalaya: The consequences of temperature and timescale on $^{40}Ar/^{39}Ar$ mica geochronology

Catherine M. Mottram [a,b,*], Clare J. Warren [a], Alison M. Halton [a], Simon P. Kelley [a], Nigel B.W. Harris [a]

[a] Department of Environment, Earth and Ecosystems, The Open University, Walton Hall, Milton Keynes, MK7 6AA, United Kingdom
[b] Department of Earth Science, University of California, Santa Barbara, 93106-9630, United States

ARTICLE INFO

Article history:
Received 28 April 2015
Accepted 28 August 2015
Available online 12 September 2015

Keywords:
$^{40}Ar/^{39}Ar$
Inverted metamorphism
Himalaya
Cooling
Ductile thrusting

ABSTRACT

$^{40}Ar/^{39}Ar$ dating of metamorphic rocks sometimes yields complicated datasets which are difficult to interpret in terms of timescales of the metamorphic cycle. Single-grain fusion and step-heating data were obtained for rocks sampled through a major thrust-sense shear zone (the Main Central Thrust) and the associated inverted metamorphic zone in the Sikkim region of the eastern Himalaya. This transect provides a natural laboratory to explore factors influencing apparent $^{40}Ar/^{39}Ar$ ages in similar lithologies at a variety of metamorphic pressure and temperature (P–T) conditions.

The $^{40}Ar/^{39}Ar$ dataset records progressively younger apparent age populations and a decrease in within-sample dispersion with increasing temperature through the sequence. The white mica populations span ~2–9 Ma within each sample in the structurally lower levels (garnet grade) but only ~0–3 Ma at structurally higher levels (kyanite-sillimanite grade). Mean white mica single-grain fusion population ages vary from 16.2 ± 3.9 Ma (2σ) to 13.2 ± 1.3 Ma (2σ) from lowest to highest levels. White mica step-heating data from the same samples yields plateau ages from 14.27 ± 0.13 Ma to 12.96 ± 0.05 Ma. Biotite yield older apparent age populations with mean single-grain fusion dates varying from 74.7 ± 11.8 Ma (2σ) at the lowest structural levels to 18.6 ± 4.7 Ma (2σ) at the highest structural levels; the step-heating plateaux are commonly disturbed.

Temperatures >600 °C at pressures of 0.4–0.8 GPa sustained over >5 Ma, appear to be required for white mica and biotite ages to be consistent with diffusive, open-system cooling. At lower temperatures, and/or over shorter metamorphic timescales, more ^{40}Ar is retained than results from simple diffusion models suggest. Diffusion modelling of Ar in white mica from the highest structural levels suggests that the high-temperature rocks cooled at a rate of ~50–80 °C Ma^{-1}, consistent with rapid thrusting, extrusion and exhumation along the Main Central Thrust during the mid-Miocene.

1. Introduction

$^{40}Ar/^{39}Ar$ dating is a tool commonly used to investigate the cooling and exhumation history of metamorphosed terranes. White mica and biotite $^{40}Ar/^{39}Ar$ ages are frequently interpreted as revealing the timing of cooling through a mineral-specific closure temperature (T_C), provided the mineral grew at a temperature considerably above the T_C (Dodson, 1973). The T_C is an estimate of the "temperature of a mineral at the time of its apparent age" (Dodson, 1973; Lister and Baldwin, 1996), and is estimated at ~470 °C for white mica and ~330 °C for biotite (100 μm grain size and cooling at 100 °C Ma^{-1}at 1 GPa, slower cooling would result in a lower T_C; Harrison et al., 2009; Harrison et al., 1985).

The "apparent" age calculated from $^{40}Ar/^{39}Ar$ data may represent a number of different processes, including, (re)crystallisation, diffusive loss of Ar during cooling, loss or gain of Ar during deformation, incorporation of excess Ar, incomplete degassing of inherited Ar, or the incomplete effects of any of the above. There are a number of assumptions that need to be met in order for an $^{40}Ar/^{39}Ar$ "date" to be interpreted as constraining the timing of cooling age following the Dodson (1973) T_C formulation. Firstly, a grain boundary fluid network must have behaved as an open system at high temperature, where Ar efficiently diffuses out of its source (the mica grain) and into the grain boundary network. As Ar is more soluble in hydrous fluid than in the crystal lattice (e.g. Kelley, 2002), and preferentially diffuses into the grain boundary network, which is assumed to represent an infinite sink. Secondly, it is assumed that there was no initial Ar within the crystal lattice when the grain (re)crystallised. Finally, it is assumed that Ar is only (re)distributed within the grain by thermally activated volume diffusion (Dodson, 1973;

* Corresponding author at: Department of Earth Science, University of California, Santa Barbara, 93106-9630, United States.
E-mail address: c.m.mottram@googlemail.com (C.M. Mottram).

http://dx.doi.org/10.1016/j.lithos.2015.08.018

Lister and Baldwin, 1996; McDougall and Harrison, 1999; Warren et al., 2012a). Furthermore, the mathematical formulation only strictly applies for a cooling path that conforms to a shape of 1/T.

Factors such as excess Ar incorporated during crystallisation, most likely facilitated by fluids (Arnaud and Kelley, 1995; Baxter et al., 2002; Di Vincenzo and Palmeri, 2001; Foland, 1979; Halama et al., 2014; Harrison et al., 1985, 2009; Itaya et al., 2009; Roddick et al., 1980; Ruffet et al., 1995), mixing of two age populations (Beltrando et al., 2009; Chopin and Maluski, 1980; Dempster, 1992; Di Vincenzo et al., 2001; Hames and Cheney, 1997; Hammerschmidt and Frank, 1991; Viete et al., 2011), and the "openness" of the grain boundary network (Kelley, 2002; Smye et al., 2013; Warren et al., 2012a) can make the interpretation of $^{40}Ar/^{39}Ar$ dates as representing crystallisation, cooling, or the partial resetting of older ages problematic. Here, "date" is used to describe apparent $^{40}Ar/^{39}Ar$ ages that have an equivocal geological meaning and "age" for those that can be linked to an event in geological time.

In this study, an inverted Barrovian metamorphic sequence associated with a major Himalayan structure, the Main Central Thrust (MCT), was exploited to investigate how the factors outlined above can influence the interpretation of $^{40}Ar/^{39}Ar$ data during Barrovian metamorphism and deformation. The inverted metamorphic sequence preserves metamorphic isograds from biotite to sillimanite grade. This represents an environment that is appropriate for the systematic investigation into how metamorphic pressures and temperatures, fluids, pervasive ductile shearing and the kinematic thrusting history impact on the apparent $^{40}Ar/^{39}Ar$ ages. Our data show that the $^{40}Ar/^{39}Ar$ populations progressively get younger, and within-sample age dispersion decreases with increasing distance and temperature through the sequence. Micas appear to require prolonged periods at moderately high metamorphic temperatures to yield robust cooling ages that can be used to estimate a cooling rate and exhumation history.

2. Geological setting

During the Eocene to recent collision of India and Asia (e.g. Najman et al., 2010 and references therein), Indian crustal rocks were buried to depths of ~20–30 km, extruded by thrusting along large-scale faults such as the Main Central Thrust (MCT) and finally exhumed to the surface. In the eastern Himalayan region of Darjeeling-Sikkim (collectively known as the Sikkim Himalaya), the MCT is exposed as a large re-entrant (>50 km across strike; Fig. 1). In this region, the MCT separates the overlying Paleoproterozoic–Neoproterozoic (~2500–800 Ma detrital zircon signature) Greater Himalayan Sequence metasediments (GHS) from the underlying Paleoproterozoic (~3600–1800 Ma detrital zircon signature) Daling Lesser Himalayan Sequence (meta)sediments (LHS) across a zone of ductile shear (Mottram et al., 2014a). Samples were collected through a transect of this zone of deformation and inverted Barrovian metamorphism developed in the MCT zone, within the Daling Formation LHS rocks (Fig. 1; Mottram et al, 2014a,b). This inverted Barrovian zone consists of an up to 5–10 km thick package of pelitic schists characterised by a well-developed penetrative schistosity (Fig. 1 and Supplementary material S2). The peak conditions of metamorphism range from ~480–530 °C and 0.5 GPa in the structurally lowermost garnet zone, ~510–565 °C and 0.4–0.6 GPa in the staurolite zone, ~565–625 °C and 0.6–0.7 GPa in the kyanite zone, ~675 °C and 0.75 GPa in the sillimanite zone and ~625–700 °C and 0.6–0.9 GPa in the structurally uppermost sillimanite K-feldspar zone (Dasgupta et al., 2004, 2009; Dubey et al., 2005; Gaidies et al., 2015). Despite preserving mineralogical assemblages typical of the Barrovian metamorphic sequence in Scotland (Barrow, 1893), the tectonic processes underpinning the formation of the Sikkim Himalayan MCT zone sequence differ from those operating during the Caledonian orogeny in Scotland (i.e. Oliver et al., 2000). Whereas metamorphism in Scotland was related to heating by fault-related mafic intrusions (i.e. Viete et al., 2011), precise geochronology shows that the inverted Barrovian sequence associated with the MCT

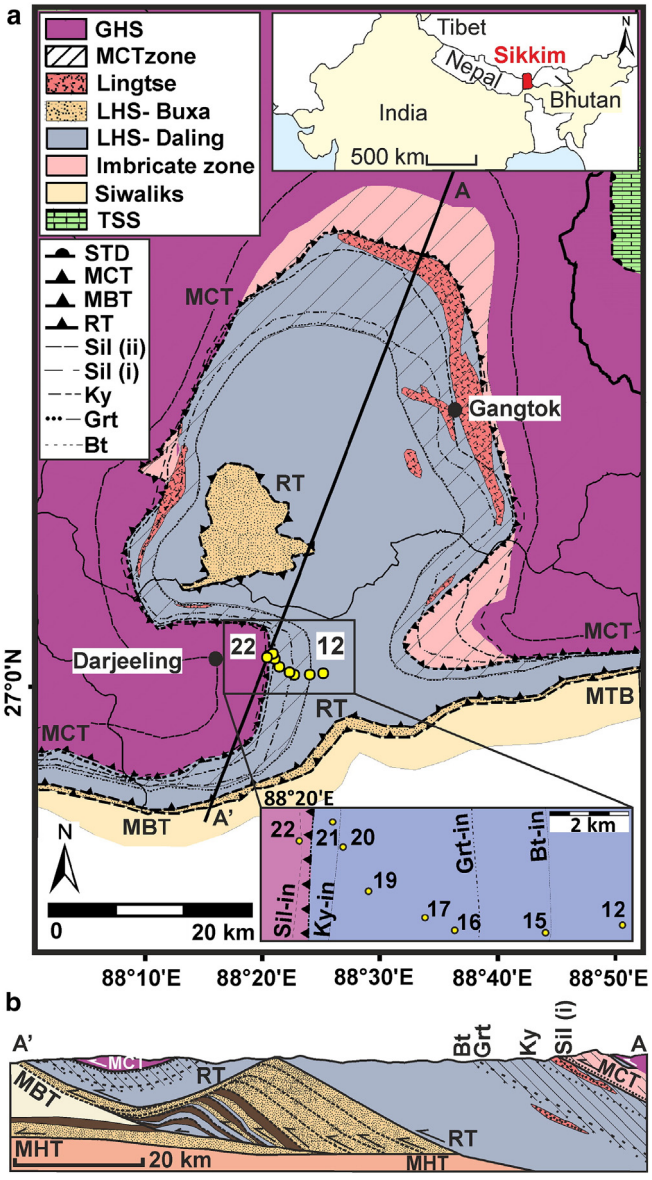

Fig. 1. Geological map (a) and cross section (b) of the Sikkim Himalaya (to scale). Adapted from Mottram et al. (2014a). Sample locations are shown in inset. Abbreviations: STD = South Tibetan Detachment, MCT = Main Central Thrust, RT = Ramgarh Thrust, MBT = Main Boundary Thrust, MHT = Main Himalayan Thrust. GHS = Greater Himalayan Sequence, LHS = Lesser Himalayan Sequence, B = Buxa, D = Daling, SW = Siwaliks, TSS = Tethyan Sedimentary Sequence. Lesser Himalayan Duplex schematic representation of Bhattacharyya and Mitra (2009). Mineral abbreviations after Whitney and Evans, 2010. The zone of deformation associated with the MCT is shown as a hatched area.

formed tectonically during ductile deformation. Metamorphism in the Sikkim Himalaya occurred contemporaneously with deformation during the progressive formation of a major mid-crustal shear zone. During ductile thrusting, the (cooler) LHS footwall material was progressively accreted to the (hotter) GHS hanging wall (i.e. Larson et al., 2013; Mottram et al., 2015). These accretion processes occurred at disparate times at different structural levels of the MCT zone and along strike in the Himalaya. In the Sikkim Himalaya prograde–peak metamorphism occurred between ~14.5 and 10.5 Ma (kyanite–garnet isograds) in the northern, rear-edge of the exposed thrust zone and between ~21 and 16 Ma (kyanite–staurolite isograds) in the southern leading edge (Anczkiewicz et al., 2014; Mottram et al., 2014b, 2015). The MCT zone in the Sikkim Himalaya was folded during formation of a late-stage duplex developed in the underlying Buxa LHS rocks, beneath the Ramgahr thrust, exposing different structural depths of the MCT (Fig. 1;

Bhattacharyya and Mitra, 2009; Mottram et al., 2014b). The timing of final exhumation of the MCT zone in the Sikkim Himalaya is poorly constrained, but it is thought to have occurred at ~10 Ma in the neighbouring Bhutan Himalaya (McQuarrie et al., 2014).

3. Petrography and mineral chemistry

3.1. Electron microprobe methods

Major-element mineral chemistry was characterised in polished sections using a Cameca SX100 (5 wavelength dispersive spectrometers) Electron Micro-Probe Analyser (EPMA) at The Open University, UK, following the method of Mottram et al., 2014b (full methods can be found in Supplementary material S1). Chemical formulae were calculated stoichometrically based on 22 oxygens for biotite and white mica. Results are presented in Table 1, Fig. 3, and Supplementary data table 1.

3.2. Sample description and mineral chemistry

The MCT transect is a pelite-rich section described in detail by Mottram et al. (2014b). Metamorphic grade increases from the structurally lowest greenschist-grade sample (12), with 1–2 mm clasts of quartz and feldspar surrounded by ~100 μm grains of white mica (full assemblage comprises white mica + quartz + plagioclase + chlorite + zircon + apatite + ilmenite + monazite − allanite reaction). Sample 15 is a fine-grained (~100 μm) chlorite–mica phyllite, with a well-developed penetrative schistosity defined by the micas in an assemblage of white mica (~100 μm) + quartz + chlorite + ilmenite + zircon + allanite + xenotime (Fig. 2).

The middle of the section is defined by garnet (staurolite)–mica schists (samples 16, 17, 19, 20 and 21) with assemblages of quartz + white mica + biotite + garnet + ilmenite ± plagioclase (sample 17, 20) ± chlorite (samples 17, 19, 20) ± K-feldspar (sample 17, 20) ± staurolite (sample 16) ± apatite (samples 16, 17, 19, 20) ± rutile (samples 17, 19, 20) ± tourmaline (samples 17, 19). In general, samples have a well-developed schistosity, which is weakly crenulated in samples 16, 17 and 19 and displays a granular texture with several mm-sized micas (which contain quartz inclusions) in sample 20. Garnet grains, which display skeletal textures in samples 17 and 21, are generally wrapped by the main penetrative foliation (defined by mica) and include micas in their inclusion trails (samples 16, 17, 19, 20, and 21). In samples 16, 17 and 19, micas have grown within garnet pressure shadows, demonstrating syn-deformation mica growth. Other samples preserve textural evidence for multiple mica populations. Subordinate clusters of white mica and biotite crystals in sample 17 are aligned oblique to the main foliation (Fig. 2), and sample 19 preserves two distinct grain sizes; a smaller fabric-forming population and larger ~0.5 mm white mica grains which cross-cut the main foliation (Fig. 2).

The structurally highest kyanite–sillimanite grade sample (sample 22) comprises the assemblage quartz + plagioclase + white mica + biotite + garnet (with mica inclusions) + kyanite + sillimanite + tourmaline + ilmenite + staurolite + rutile + apatite. The sample is a coarse-grained schist, which displays a weak schistosity defined by white mica (~8 mm long). Full petrological descriptions and photomicrographs of all samples can be found in Fig. 2 and in Supplementary material S2.

White mica compositions are fairly uniform within each sample. For all samples, Si ions per formula unit (pfu) range from 6.2–6.42; Na/(Na + K) ratios range from 0.02–0.2, and Ti ions pfu range from 0.03–0.10 (Fig. 3; Table 1; Supplementary data table 1).

Biotite compositions are also fairly uniform in all samples, with Si ions ranging from 5.52 to 6.25 pfu; Ti ions from 0.18 to 0.32 pfu; XFe (Fe/(Fe + Mg)) from 0.55 to 0.63; and XMg (Mg/(Mg + Fe) from 0.37 to 0.5. The Ti content of both white mica and biotite is lower at lower metamorphic grade. This is particularly noticeable in biotite analyses, for which Ti ion content varies from ~0.2 to 0.4 pfu for the higher-grade samples (samples 19–22) and 0.15–0.2 pfu for the lower grade samples (samples 16 and 17; Fig. 3; Table 1; Supplementary data table 1).

Table 1
Average chemical composition of white mica (WM) and biotite (Bt) grains dated in each sample. Full dataset in Supplementary material S2.3 and in supplementary data.

Sample	12	15	16	16	17	17	19	19	20	20	21	21	22	22
	WM	WM	WM	Bt	WM	Bt	WM	Bt	WM	Bt	WM	Bt	WM	Bt
SiO_2	45.73	46.19	46.15	35.72	46.71	36.42	47.52	35.75	46.51	35.02	48.60	35.27	46.19	35.82
TiO_2	0.50	0.26	0.40	1.51	0.61	1.57	0.99	2.63	1.02	2.74	0.87	2.76	0.88	2.54
Al_2O_3	29.04	33.00	34.05	18.55	34.15	18.13	33.44	18.94	34.00	18.67	32.62	17.96	34.56	19.46
Cr_2O_3	0.02	0.01	0.02	0.02	0.02	0.00	0.03	0.02	0.02	0.03	0.02	0.02	0.01	0.03
MgO	1.78	0.85	0.72	8.92	0.99	10.30	1.04	8.41	0.85	7.31	1.25	7.60	0.81	8.60
CaO	0.03	0.05	0.01	0.03	0.03	0.06	0.02	0.05	0.02	0.06	0.00	0.02	0.01	0.05
MnO	0.03	0.01	0.00	0.01	0.00	0.01	0.01	0.01	0.01	0.14	0.01	0.24	0.01	0.09
FeO	4.46	2.65	1.71	20.08	1.28	18.34	1.52	18.97	1.43	22.00	1.84	21.00	1.19	19.02
Na_2O	0.31	0.77	1.12	0.28	1.52	0.21	0.24	0.08	0.77	0.12	0.17	0.09	1.06	0.20
K_2O	10.34	9.21	9.42	8.29	8.96	8.89	10.68	8.32	9.82	8.77	11.03	9.41	9.39	8.26
F	0.13	0.13	0.09	0.21	0.09	0.31	0.09	0.22	0.06	0.13	0.11	0.18	0.10	0.23
Cl	0.00	0.02	0.02	0.03	0.00	0.02	0.00	0.02	0.00	0.01	0.00	0.03	0.00	0.00
Total	92.36	93.15	93.70	93.64	94.35	94.26	95.57	93.40	94.50	95.01	96.52	94.59	94.21	94.29
Cations per 22 O														
Si	6.42	6.31	6.25	5.54	6.25	5.59	6.32	5.52	6.24	5.42	6.42	5.49	6.20	5.48
Ti	0.05	0.03	0.04	0.18	0.06	0.18	0.10	0.30	0.10	0.32	0.09	0.32	0.09	0.29
Al	4.80	5.31	5.43	3.39	5.39	3.28	5.20	3.41	5.37	3.40	5.08	3.29	5.47	3.51
Cr	0.00	0.00	0.00	0.00	0.00	0.00	0.00	0.00	0.00	0.00	0.00	0.00	0.00	0.00
Mg	0.37	0.17	0.14	2.06	0.20	2.35	0.20	1.91	0.17	1.69	0.25	1.76	0.16	1.96
Ca	0.00	0.01	0.00	0.00	0.01	0.01	0.00	0.01	0.00	0.01	0.00	0.00	0.00	0.01
Mn	0.00	0.00	0.00	0.00	0.00	0.00	0.00	0.00	0.00	0.02	0.00	0.03	0.00	0.01
Fe	0.52	0.30	0.19	2.60	0.14	2.35	0.17	2.42	0.16	2.85	0.20	2.73	0.13	2.43
Na	0.08	0.20	0.29	0.08	0.39	0.06	0.06	0.02	0.20	0.04	0.04	0.03	0.28	0.06
K	1.85	1.60	1.63	1.64	1.53	1.74	1.80	1.62	1.68	1.73	1.86	1.87	1.61	1.61
F	0.06	0.05	0.04	0.10	0.04	0.15	0.04	0.11	0.02	0.06	0.05	0.09	0.04	0.11
Cl	0.00	0.00	0.00	0.01	0.00	0.01	0.00	0.00	0.00	0.00	0.00	0.01	0.00	0.00
Total	14.18	14.00	14.02	15.62	14.01	15.72	13.89	15.33	13.95	15.54	13.98	15.63	13.98	15.48
Na/Na + K	0.04	0.11	0.15	0.05	0.20	0.03	0.03	0.01	0.11	0.02	0.02	0.02	0.15	0.04
XMg	0.42	0.36	0.42	0.44	0.59	0.5	0.54	0.44	0.52	0.37	0.56	0.39	0.55	0.45
XFe	0.58	0.64	0.58	0.56	0.41	0.50	0.46	0.56	0.48	0.63	0.44	0.61	0.45	0.55

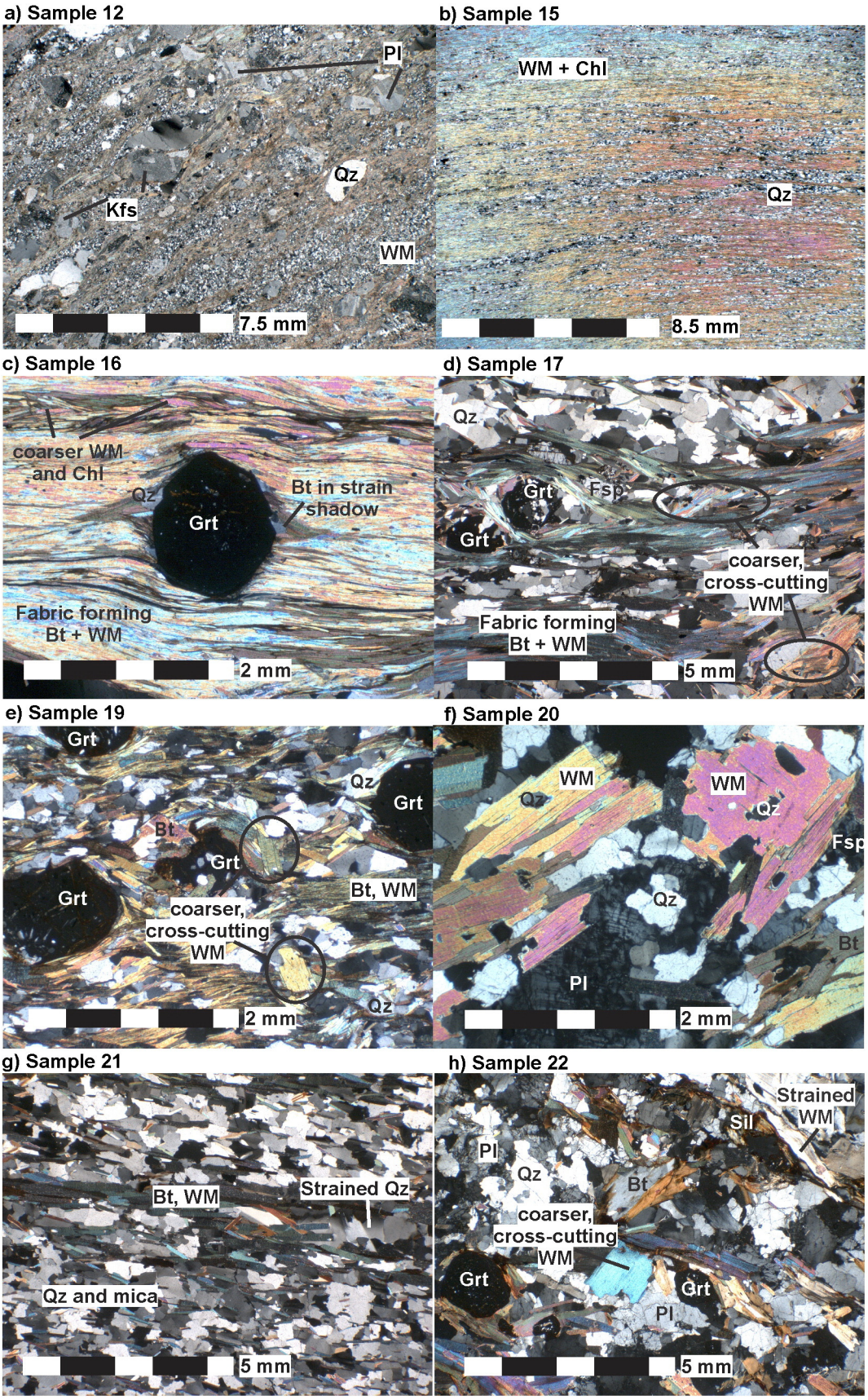

Fig. 2. Photomicrographs of thin section through crossed polars. Mineral abbreviations after Whitney and Evans (2010). WM = white mica.

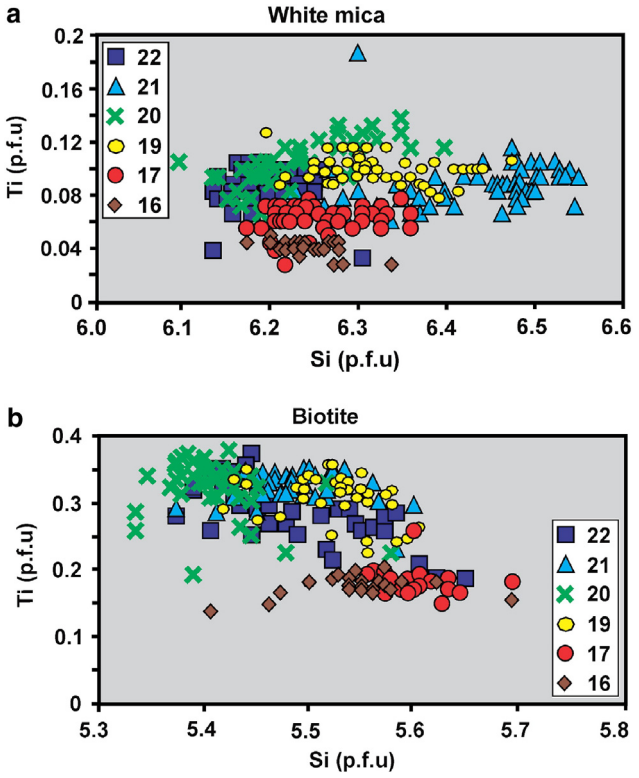

Fig. 3. White mica (a) and biotite (b) geochemistry. Errors are encompassed within the symbols.

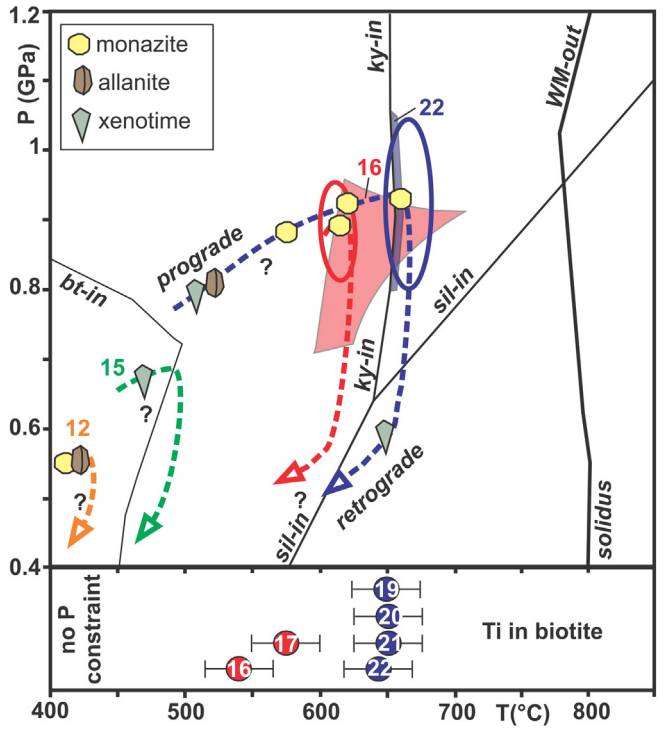

Fig. 4. Summary of P–T conditions. Coloured arrows represent the P–T path for each sample which are approximated from average P–T, Ti-in-biotite, accessory phase analysis and pseudosection analysis (taken from Mottram et al., 2014b). Temperatures from Ti in biotite with 50 °C error bars are shown in the bottom panel (independent of pressure). Ellipses/shaded areas show peak P–T fields from pseudosection analysis for samples 16 and 22 (Mottram et al., 2014b). For interpretation of the references to colour in this figure legend, the reader is referred to the web version of this article.

4. P–T conditions

4.1. Average P–T methods

P–T estimates were calculated using the Ti-in-biotite (TiB) calculation of Henry et al. (2005), the phengite geobarometer of Massonne and Schreyer (1987), the garnet–biotite thermometer of Bhattacharya et al. (1992) and the garnet–Al_2SiO_5–plagioclase (GASP) barometer of Powell and Holland (1988); summarised in Fig. 4). The precision on the original TiB calibration is estimated at ±12 °C (Henry et al., 2005) at high temperatures. A larger uncertainty (±50 °C) was applied in this study to account for biotite crystallisation outside the 0.3–0.6 GPa calibration range of the thermometer (cf. Warren et al., 2014). Analysis of accessory phases (Fig. 5) also allowed additional P–T information to be obtained for samples lacking the appropriate major phases for average P–T estimates.

4.2. P–T results

4.2.1. Thermobarometry

The Ti-in-biotite temperatures vary from 545 ± 50 °C for (structurally lowest) sample 16 to 652 ± 50 °C for (structurally highest) sample 22 (Mottram et al., 2014b; Table 2; Fig. 4; Supplementary material S3.1).

The K-feldspar–quartz–phlogopite barometer (Massonne and Schreyer, 1987) yields white mica pressures of ~0.5 GPa (Table 2) for samples 17 and 20 (the only samples containing the K-feldspar required for the calibration).

The garnet–biotite geothermometer yields temperatures ranging from 530 ± 50 °C for sample 16 to 687 ± 50 °C for sample 22 (Table 2; Fig. 4). A pressure estimate of 0.9 GPa was obtained for sample 22, the only sample that contains an aluminosilicate phase.

4.2.2. Accessory phase analysis

The appearance and disappearance of accessory phases can help constrain conditions of metamorphism in samples that do not contain the correct mineral assemblage for conventional P–T modelling. Previous studies have shown that, at greenschist facies conditions, detrital monazite (sample 12; Fig. 5 and Supplementary material S3.2) dissolves to form low-Th metamorphic monazite and allanite (Gasser et al., 2012; Janots et al., 2008; Krenn and Finger, 2007; Rasmussen and Muhling, 2009; Smith and Barreiro, 1990). This texture was observed in sample 12 (Fig. 5), which is therefore inferred to have formed at ~400 °C (cf. Janots et al., 2007).

Xenotime can similarly form from the breakdown of detrital monazite in Al-rich rocks around the biotite isograd (~430–450 °C; Janots et al., 2008). This reaction provides temperature constraints on the formation of sample 15 (Fig. 5; Janots et al., 2008; Smith and Barreiro, 1990).

5. Geochronology

5.1. $^{40}Ar/^{39}Ar$ methods

Single-grain fusion (sgf), *in-situ* laser ablation and laser multi-grain step-heating analyses were performed at The Open University, UK. Full methods are provided in Supplementary material S1. The benefit of collecting Ar data by both sgf and step-heating methods is that dating individual grains by sgf can reveal inter-grain age heterogeneity that may otherwise be masked by step-heating. The sgf dataset thus helps to provide an explanation for any discordance in step-heating results.

The lowest metamorphic grade samples (samples 12 and 15) were analysed by *in-situ* laser ablation on polished slabs, due to the fine-grained nature of the sample material. Samples 16–22, with grains

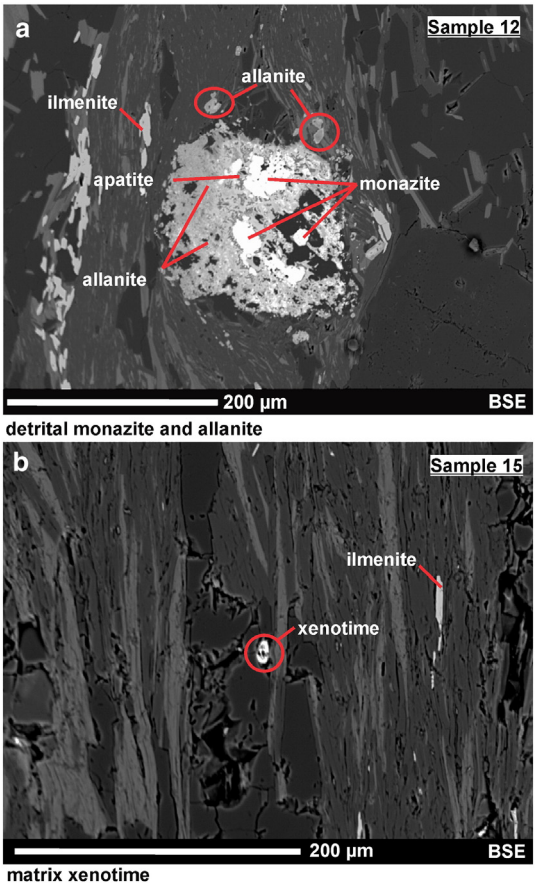

Fig. 5. Backscatter images of accessory phases in selected samples.

large enough to be separated, were crushed, washed and sieved, and ~20 grains of the least-deformed, most inclusion-free white mica and biotite grains of ~0.5–1 mm diameter were picked for each sgf and step-heating analysis (images of samples in Supplementary material S4.1). Grains were washed in acetone, and distilled water before packing into aluminium foil packets for irradiation.

All samples were irradiated at McMaster University, Canada. Irradiation flux was monitored using the GA1550 biotite standard with an age of 99.77 ± 0.11 Ma (Renne et al., 2010). Sample J-values (Supplementary data table 2) were calculated by linear interpolation between two bracketing standards; a standard was included between every 8–10 samples in the irradiation tube.

Ar isotope data were collected using a Nd-YAG 1064 nm infra-red laser coupled to an automated gas handling vacuum system and admitted into an MAP 215-50 noble gas mass spectrometer. Data were reduced using an in-house software package (ArMaDiLo), and plotted using Isoplot (Ludwig, 2003).

All analyses were corrected for background decay of ^{37}Ar and ^{39}Ar and neutron-induced interference reactions using correction factors of $(^{40}Ar/^{39}Ar)_K = 0.0085$; $(^{39}Ar/^{37}Ar)_{Ca} = 0.00065 \pm 0.0000033$ and $(^{36}Ar/^{37}Ar)_{Ca} = 0.000264 \pm 0.000001$, which were determined from analyses of K_2SO_4/ CaF_2 salts. All analyses were corrected for machine background (one measurement for every 1–2 standards/sample measurements); typical values for each sample run are included in Supplementary data table 2. Analyses were also corrected for mass spectrometer discrimination using a value of 283 for the $^{40}Ar/^{36}Ar$ ratio, determined from routine analyses of modern glass. Atmospheric Ar contents were measurable on larger samples and were generally <5% of the total ^{40}Ar (Supplementary data table 2). Samples were corrected for atmospheric Ar contamination using a $^{40}Ar/^{36}Ar$ ratio of 298.56 (Lee et al., 2006). Data are presented at the 95% confidence level, all dates are quoted at 2σ and uncertainties on measurements are 1σ. The $^{40}K/^{40}Ar$ decay constant of Min et al. (2000) was used throughout.

For step-heating experiments, plateaux were defined by at least three consecutive steps containing a minimum of 50% of the total ^{39}Ar release (e.g. Kula et al., 2010). Where the ^{39}Ar release was <50%, and therefore the statistical criteria for a plateau age were not met, an Isoplot (Ludwig, 2003) weighted average of the most concordant portion of the release spectra was calculated.

5.2. $^{40}Ar/^{39}Ar$ results

The full white mica and biotite single-grain fusion (sgf) and step-heating results are summarised in Figs. 6–8 and Table 3. Full data tables, inverse isochron plots and weighted average calculations and combined data plots are provided in Supplementary data table 2 and Supplementary material S4.

The *in-situ* laser spot analyses of low-grade samples (samples 12 and 15) yielded $^{40}Ar/^{39}Ar$ dates that vary from 1290 ± 40 Ma to 53 ± 5 Ma for sample 12 (with an additional meaningless date of 5300 ± 134 Ma) and between 109 ± 6 Ma and 16 ± 1 Ma for sample 15.

White mica $^{40}Ar/^{39}Ar$ dates (Figs. 6–8; Table 3) range from 18.96 ± 2.71 Ma to 14.16 ± 1.62 Ma (sgf data), with a weighted average of 16.3 ± 1.3 Ma (MSWD = 0.8) in the lowest-grade sample (sample

Table 2
Ti in biotite, average P–T and accessory phase results.

Sample	Ti in biotite (°C)[a]	Phengite barometer (GPa)[b]	Garnet–biotite temperature (°C)[c]	GASP pressure (GPa)[d]	Accessory phase temperature estimate (°C)[e]	Pseudosection peak field[f]
12	nd	nd	nd	nd	~400	nd
15	nd	nd	nd	nd	~430–450	nd
16	545	nd	531	nd	nd	~580 °C/0.8 GPa
17	570	~0.5	580	nd	nd	nd
19	649	nd	627	nd	nd	nd
20	652	~0.5	630	nd	nd	nd
21	652	nd	nd	nd	nd	nd
22	643	nd	687	0.9	nd	~650 °C/0.8 GPa

nd = not determined due to lack of one or more critical phases.
[a] Henry et al. (2005) (±50 °C).
[b] Massonne and Schreyer (1987).
[c] Bhattacharya et al. (1992) ±50 °C.
[d] Powell and Holland (1988) ± 0.1 GPa.
[e] Based on Smith and Barreiro, 1990; Janots et al., 2007 and Janots et al., 2008.
[f] Published in Mottram et al. (2014b).

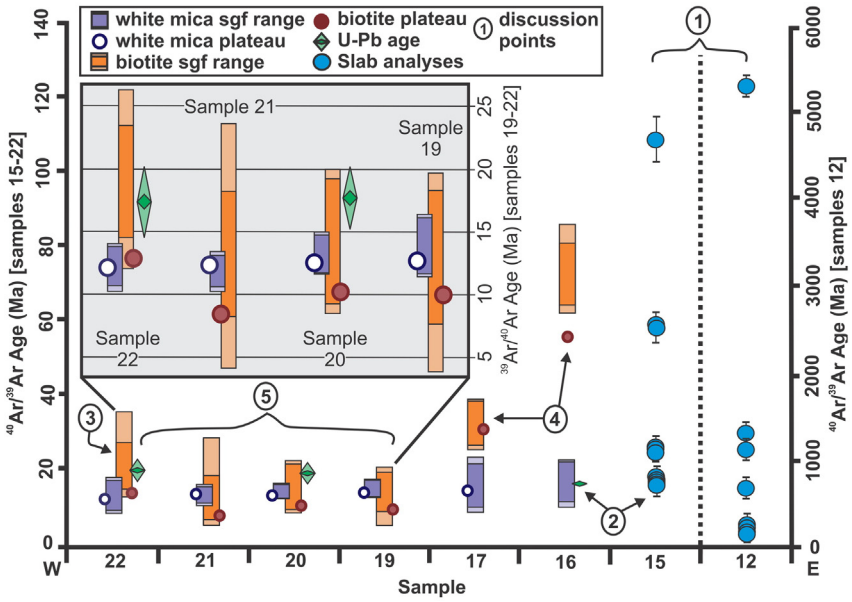

Fig. 6. Summary of ^{40}Ar/^{39}Ar mica and U–Pb zircon data. Monazite U–Th–Pb data taken from Mottram et al. (2014b). Sample 12 is plotted according to right-hand scale. Error bars are 2σ and incorporate uncertainties in J-values.

16—analysed for sgf and step-heating analysis); step-heating analysis yielded discordant release spectra in sample 16. Sample 17 yielded sgf dates from 17.83 ± 2.44 Ma to 12.07 ± 1.36 Ma, with a weighted average of 14.4 ± 1.2 Ma (MSWD = 1.9). Step-heating analysis yielded a statistically identical concordant plateau date of 14.27 ± 0.13 Ma (MSWD = 1.3, 80% ^{39}Ar). White mica sgf dates in sample 19 range from 16.34 ± 0.86 Ma to 12.95 ± 0.46 Ma, with a weighted average of 13.7 ± 1 Ma (MSWD = 2.6) and yield a statistically identical step-heating plateau date of 13.47 ± 0.21 Ma (MSWD = 0.7, 57% ^{39}Ar). In sample 20, white mica sgf dates range from 14.89 ± 0.90 Ma to 13.12 ± 0.85 Ma, with a weighted average of 13.7 ± 0.5 Ma (MSWD = 0.6), and yield a statistically identical step-heating plateau date of 13.36 ± 0.07 Ma (MSWD = 1.2, 99.5% ^{39}Ar). White mica sgf dates in sample 21 range from 13.32 ± 0.50 Ma to 12.02 ± 0.93 Ma, with a weighted average of 12.7 ± 0.3 Ma (MSWD = 0.3), and yield a statistically identical step-heating date of 13.10 ± 0.05 Ma (MSWD = 1.2, 100% ^{39}Ar). In the highest-grade sample (sample 22), white mica sgf dates range from 14.00 ± 0.88 Ma to 11.99 ± 0.93 Ma, with a weighted average of 13.3 ± 0.5 Ma (MSWD = 0.5). Step-heating analysis yielded a statistically identical plateau date of 12.96 ± 0.05 Ma (MSWD = 1.6, 100% ^{39}Ar).

Biotite ^{40}Ar/^{39}Ar dates (Figs. 6–8; Table 3) range from 79.51 ± 13.32 Ma to 66.25 ± 2.35 Ma in the lowest-grade sample (sample 16), with a weighted average of 71.0 ± 6.9 Ma (MSWD = 2.8). In sample 17, sgf dates range from 37.38 ± 1.51 Ma to 27.36 ± 1.00 Ma, with a weighted average date of 31.9 ± 4.0 Ma (MSWD = 9.5). Samples 16 and 17 both yielded discordant step-heating release spectra for biotite. Biotite sgf dates in sample 19 range from 18.47 ± 1.99 Ma to 9.08 ± 4.40, with a weighted average of 16.0 ± 2.2 Ma (MSWD = 2.6). Step-heating analysis yielded a plateau date of 10.83 ± 0.34 Ma (MSWD = 1.2, 58% ^{39}Ar). In sample 20, sgf dates range from 19.39 ± 1.43 Ma to 10.67 ± 1.34 Ma, with a weighted average of 12.7 ± 1.2 Ma (MSWD = 4). Step-heating analysis yielded a discordant release spectrum. Biotite sgf dates in sample 21 range from 18.43 ± 6.00 Ma to 9.68 ± 4.74 Ma, with a weighted average of 12.6 ± 1.1 Ma (MSWD = 0.7). The step-heating analysis yielded a plateau date of 9.26 ± 0.27 Ma (MSWD = 1.8, 79% ^{39}Ar). Sample 22, from the highest grade in this transect, yielded sgf dates that range from 23.60 ± 3.54 Ma to 15.86 ± 3.04 Ma, with a weighted average of 18.3 ± 1.0 Ma (MSWD = 0.9). Step-heating analysis yielded a discordant release spectrum.

5.3. Zircon U–Pb methods

Zircon was analysed using a Nu Plasma HR multi-collector inductively coupled plasma mass spectrometer (MC-ICP-MS) (Nu Instruments, Wrexham, UK) and a UP193FX (193 nm) excimer or UP193SS (193 nm) Nd:YAG laser ablation system (New Wave Research, UK), at The NERC Isotope Geosciences Laboratory (NIGL), UK. Analyses followed the method of Mottram et al. (2014a); full analytical conditions are given in Supplementary material S1. All data, quoted at the 2σ confidence level, are shown in Supplementary data table 3.

5.4. U–Pb results

U–Pb zircon data for sample 20 are shown in Fig. 9 and all zircon images shown in Supplementary material S5. Zircon rims yield ages that range from ~21 to 16 Ma. These data complement a published U–Th–Pb monazite dataset from additional samples collected from the same transect (Mottram et al., 2014b; Table 3).

6. Discussion

6.1. Critical evaluation of the data

Both white mica and biotite ^{40}Ar/^{39}Ar populations get younger with increasing up-section temperature (Figs. 6–8). Mica mats from the lowest structural levels (samples 12 and 15), yield anomalously old dates that almost certainly do not relate to the timing of the Himalayan orogen (discussion point 1, Fig. 6; Section 6.1.1). These samples underwent a relatively short period of peak metamorphic heating at ~16 Ma, under temperature conditions of ~400 °C (Mottram et al., 2014b). Further up-section, above the garnet isograd (~580 °C; samples 16–17), the fabric-forming white mica population yield mean sgf dates of 16.2 ± 3.9 Ma, which overlap with U–Pb ages, indicating that the Ar dates could represent crystallisation ages (discussion point 2, Fig. 6; Section 6.1.2). These samples, however, yield highly dispersed ^{40}Ar/^{39}Ar dates (~5 Ma in white mica and ~9–13 Ma in biotite — Table 3 and Figs. 6–8), and discordant step-heating spectra, suggesting a source of excess Ar, from a retained "Ar memory" (discussion point 4, Fig. 6; Section 6.1.4). Biotite sgf and plateau dates alternate between yielding older (samples 16, 17, and 22) and younger (samples 19–21)

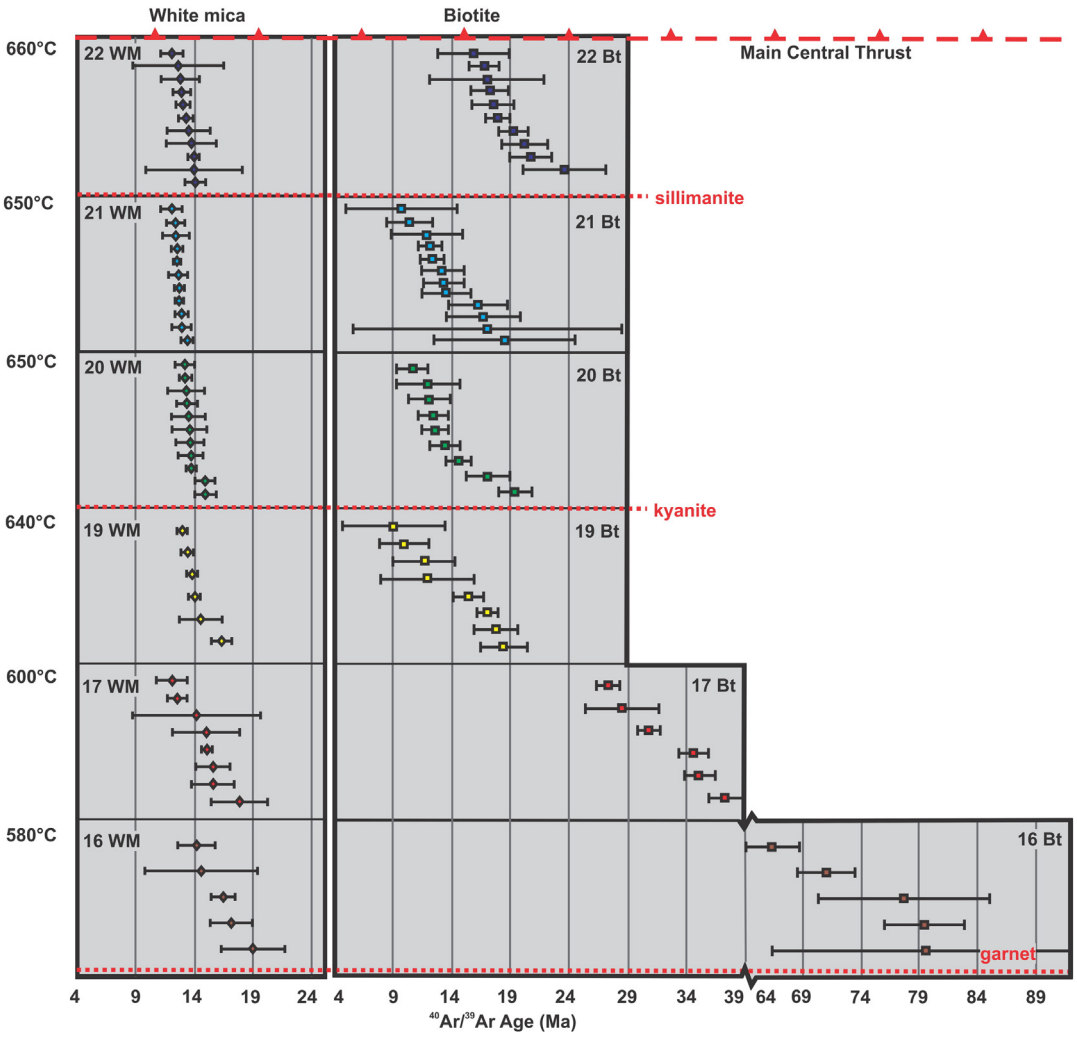

Fig. 7. Detailed summary of white mica and biotite single-grain fusion data. White mica grains are shown as diamonds, biotite grains as boxes. Error bars are 2σ and incorporate uncertainties in J-values. Garnet, kyanite and sillimanite isograds are shown in red and temperature constraints are approximated from P–T data summarised in Fig. 4. For interpretation of the references to colour in this figure legend, the reader is referred to the web version of this article.

dates than their white mica counterparts, a trend possibly explained by the influence of deformation or contamination by extraneous Ar (discussion points 3–4, Fig. 6; Sections 6.1.3–4). In the structurally highest parts of the section (samples 19–22), which experienced prolonged periods at temperatures of ~650 °C between ~21 and 16 Ma (zircon data from this study; Mottram et al., 2014b), white mica $^{40}Ar/^{39}Ar$ sgf and step-heating data consistently yield narrow age populations (mean fabric-forming white mica sgf dates of 13.2 ± 1.3 Ma) and plateaux at ca. 13 Ma. As these grains experienced temperatures conducive for diffusive, open-system cooling, these dates are interpreted as representing cooling ages (discussion point 5, Fig. 6; Section 6.1.5). Our results suggest that both the residence time and thermal conditions experienced by micas are critical for open-system behaviour.

6.1.1. Detrital ages

The lowest-grade samples (samples 12 and 15), yield dates that are pre-Himalayan, and in the case of sample 12, clearly anomalous (discussion point 1, Fig. 6). Some individual dates from samples 12 and 15 may represent detrital crystallisation ages, or partially reset detrital ages, however, these dates are inconsistent with ages obtained from other detrital geochronometers such as zircon (Mottram et al., 2014a), and dissimilar to any previously known geological events in the Himalaya. The analyses carry large uncertainties due to the low volumes of Ar release, likely caused by a lack of spatial precision on the fine-grained mats and consequent coeval analysis of low-K materials such as fluid inclusions or quartz (Supplementary data table 2). This is potentially the cause of both the erroneous results and the large errors, although we cannot rule out contamination of these samples by inherited or excess Ar.

6.1.2. Crystallisation ages

Rocks within the MCT shear zone experienced a prolonged (several Ma) period of coeval metamorphism and deformation, as evidenced by the ~21–16 Ma prograde to peak monazite ages reported by Mottram et al. (2014b), constraining the timing of the high-temperature portion of the metamorphic cycle. Textural evidence suggests that micas were present and stable in all samples throughout the metamorphic and deformation history of the MCT. The yielded range of sgf dates (Fig 7.) could therefore represent mica crystallisation ages throughout the prograde, peak and retrograde metamorphic history.

Inclusions of biotite and white mica in garnet (samples 16, 17, 19, 20, 21, and 22) suggest that both were present in the assemblage during the prograde evolution. Both white mica and biotite are the dominant fabric-forming phase in all samples. Micas wrapping around garnets and subordinate post-kinematic cross-cutting grains provide textural evidence for mica forming mainly as part of the thermal peak assemblage.

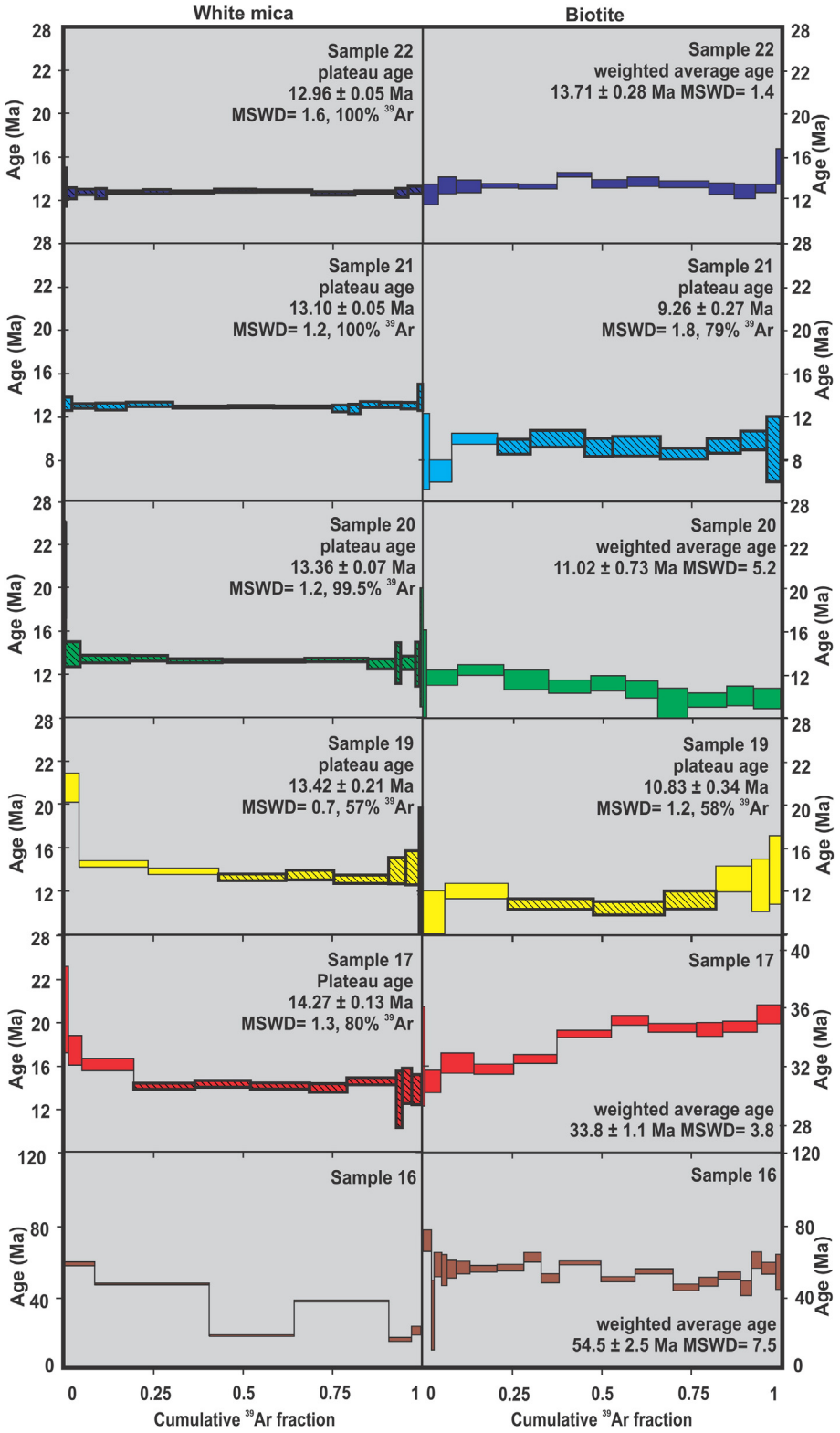

Fig. 8. Summary of white mica and biotite $^{40}Ar/^{39}Ar$ step-heating data. Error bars are 2σ and incorporate uncertainties in J-values. Plateaus are defined by amount of gas shown as percentage. Weighted averages are calculated for the 'plateau' regions of each sample array using Isoplot (Ludwig, 2003; Supplementary material S4.3).

There is little chemical variation within and between micas from the same sample, with variations only existing between samples formed at different temperatures (particularly in Ti content). This suggests that micas within each sample either continuously recrystallised during the prograde–retrograde path, or that they all formed in equilibrium within a given sample. The chemical composition of the fabric-forming micas is consistent with growth at peak conditions because (i) at lower structural levels there is consistency between Ti-in-biotite and garnet–biotite thermometry results (i.e. sample 16), and (ii) at higher structural levels, Ti-in-biotite temperatures are consistent with pseudosection peak fields (i.e. sample 22; Table 2; Mottram et al,., 2014b). A lack of high-spatial (intragrain,

Table 3
Summary of white mica (WM) and biotite (Bt) sgf and step-heating experiment results and monazite–zircon U–Pb age and difference in cooling (Ar) and peak (U–Pb) age.

Sample	sgf (Ma)									Step-heating (Ma)		Mnz/Zrn age (Ma)	Diff. peak and cooling age (best; Ma)
	WM minimum age	WM maximum age	WM wtd average age (MSWD)	WM mean age (2SD error)	WM range[a]	Bt minimum age	Bt maximum age	Bt wtd average age (MSWD)	Bt mean age (2SD error)	Bt range[a]	WM plateau age (MSWD)	Bt plateau age (MSWD)		
16	14.2 ± 1.6	19 ± 2.7	16.3 ± 1.3 (0.8)	16.2 ± 3.9	4.8	66.3 ± 2.4	79.5 ± 13.3	71 ± 6.9 (2.8)	74.7 ± 11.8	13.2	none	54.2 ± 2.5 (7.5)[b]	15.9 ± 0.3[c]	1.7 ± 1.7
17	12.1 ± 1.4	17.8 ± 2.4	14.4 ± 1.2 (1.9)	14.7 ± 3.7	5.1	27.4 ± 1	37.4 ± 1.5	31.9 ± 4 (9.5)	32.3 ± 8	10	14.27 ± 0.13 (1.3)	33.8 ± 1.1 (3.8)[b]	Assuming ~16	1.7 ± 0.5
19	13 ± 0.5	16.3 ± 0.9	13.7 ± 1 (2.6)	14.2 ± 2.4	3.3	9.1 ± 4.4	18.5 ± 2	16 ± 2.2 (2.6)	14 ± 7.2	9.4	13.42 ± 0.21 (0.7)	10.83 ± 0.34 (1.2)	Assuming ~16	2.6 ± 0.5
20	13.1 ± 0.9	14.9 ± 0.9	13.7 ± 0.5 (0.6)	13.7 ± 1.2	1.8	10.7 ± 1.3	19.4 ± 1.4	13.8 ± 2 (3.5)	13.8 ± 5.6	8.7	13.36 ± 0.07 (1.2)	11.02 ± 0.73 (5.2)[b]	~16 – 21[d]	2.6 ± 0.5
21	12 ± 0.9	13.3 ± 0.5	12.7 ± 0.3 (0.3)	12.6 ± 0.7	1.3	9.7 ± 4.7	18.4 ± 6	12.6 ± 1.1 (0.7)	13.7 ± 5.5	8.7	13.1 ± 0.05 (1.2)	9.26 ± 0.27 (1.8)	Assuming ~16	2.9 ± 0.5
22	12 ± 0.9	14 ± 0.9	13.3 ± 0.5 (0.5)	13.2 ± 1.3	2	15.9 ± 3	23.6 ± 3.5	18.3 ± 1 (0.9)	18.6 ± 4.7	7.7	12.96 ± 0.05 (1.6)	13.71 ± 0.28 (1.4)[b]	15.6 ± 0.2- 20.8 ± 0.2[c]	2.6 ± 0.3

[a] Range = difference between maximum and minimum mica ages.
[b] weighted average.
[c] Results from Mottram et al. (2014b).
[d] Zircon results from this study, with youngest zircon age used in calculations.

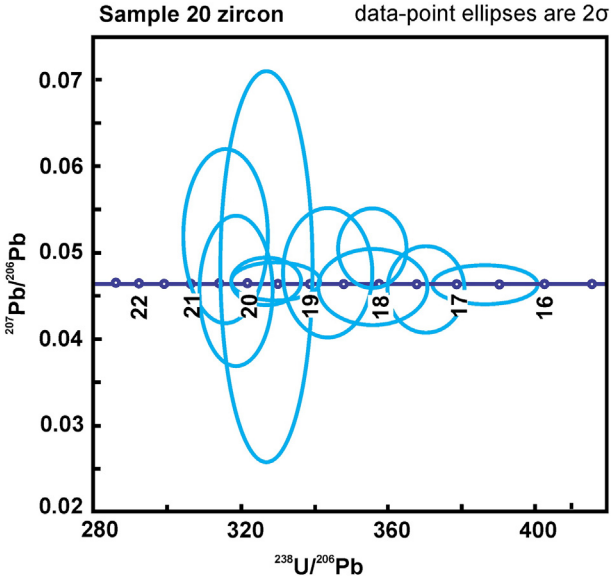

Fig. 9. Tera–Wasserburg zircon U–Pb data plot for sample 20 (Ludwig, 2003) with 2σ error ellipses.

in-situ) $^{40}Ar/^{39}Ar$ data means that linking age to textural location is impossible.

In-situ analyses of white mica mats in sample 15, white mica separates from samples 16 and 17, and biotite separates from sample 19 yield Ar dates that, on average, are younger than the monazite ages (discussion point 2, Fig. 6), and are thus more consistent with either an interpretation of mica (re)crystallisation during peak conditions or post-peak recrystallisation (e.g. Dunlap, 1997; Dunlap et al., 1991; Kirschner et al., 1996). Fine-grained mica mats within sample 15 provide textural evidence for possible recrystallisation. This sample, however, also yields a range of older sgf dates, the oldest of which is too old to be interpreted as a crystallisation age, yet not old enough to be interpreted as a detrital age (~109 Ma). Overall these age populations suggest incomplete degassing of inherited Ar, or contamination by excess Ar.

6.1.3. Deformation-related ages

It has been shown that deformation of the crystal lattice can cause dislocations within grains that can reduce the diffusion length scale for ^{40}Ar in a grain (Cosca et al., 2011), act as a network for intragrain loss of radiogenic Ar (Kramar et al., 2001), act as a pathway for the ingress of external ^{40}Ar, and provide a trapping mechanism for internal ^{40}Ar (Reddy et al., 2001). Post-crystallisation deformation could therefore play an important role in the efficiency of Ar removal, and provide a mechanism for perturbing the Ar concentrations in the micas. Microstructural deformation leading to the trapping of ^{40}Ar may have occurred in some of the Sikkim Himalayan rocks. There is however scant microtextural evidence for mica deformation; samples 16–19 contain a crenulated cleavage, but individual grains are largely undeformed. In sample 22 undulose extinction textures present in larger biotite and white mica grains may provide an explanation for some of the anomalously old dates yielded by biotite (Fig. 2 and discussion point 3, Fig. 6; Supplementary material S2.2).

6.1.4. Excess Ar

The sgf data show that biotite grains consistently yield older dates (samples 16, 17, and 22) and/or a larger dispersion than the white mica grains in the same sample. This is the antithesis of what would be predicted on the basis of loss by diffusion, as biotite is suggested to be less retentive than white mica (McDougall and Harrison, 1999). Biotite commonly yields older ages than white mica grains in Himalayan

samples, and the widely held interpretation is that excess Ar is the cause (Copeland et al., 1991; Godin et al., 2001; Hubbard and Harrison, 1989; Macfarlane, 1993; Stüwe and Foster, 2001). Minerals such as biotite, white mica and chlorite are known to be able to incorporate excess Ar into their mineral structures, either during crystallisation or due to post-crystallisation interaction with fluids (Arnaud and Kelley, 1995; Di Vincenzo and Palmeri, 2001; Foland, 1979; Roddick et al., 1980; Ruffet et al., 1995). Biotite and chlorite are probably the largest sink for grain-boundary-hosted Ar, as they have relatively open crystal lattices and are thus the most receptive to incorporation of external Ar (Jackson et al., 2013; Wartho et al., 2013). White mica can also incorporate excess Ar into its structure, but likely in less significant amounts than coexisting biotite (Brewer, 1969). The older and more dispersed dates in biotite compared to those obtained from white mica therefore suggest that excess Ar was prevalent in the grain boundary network at temperatures below the white mica T_C. Alternatively, as solubility of Ar in biotite is much greater than for white mica the biotite may have been preferentially contaminated by excess Ar during (re)crystallisation, (e.g. Brewer, 1969; Dahl, 1996; Roddick et al., 1980).

The presence or absence of excess Ar may be assessed by plotting step-heating data on inverse isochron plots (Supplementary material S4.2). The initial $^{36}Ar/^{40}Ar$ ratios of our samples generally lie within uncertainty of the atmospheric ratio of 0.00335 ± 0.000006 (Lee et al., 2006). However, low ^{36}Ar concentrations in most analyses have led to large uncertainties on the initial $^{40}Ar/^{36}Ar$ ratio, thus making these plots of limited interpretive use.

The difference between the biotite and white mica $^{40}Ar/^{39}Ar$ populations is much larger at the lower structural levels than at the upper levels (samples 16–17; discussion point 4, Fig. 6). Fluids produced during metamorphic reactions could have transported Ar (produced elsewhere) into the local rock volume (Arnaud and Kelley, 1995; Di Vincenzo and Palmeri, 2001; Foland, 1979; Roddick et al., 1980). Differential fluid flow within the shear zone can explain the trend of older dates at structurally lower levels.

6.1.5. Thermal diffusion

The T_C approach (Dodson, 1973), is based on assumptions about the diffusion characteristics of Ar relative to the sample P–T history. The calculation assumes that cooling starts from infinite temperatures and that $^{40}Ar/^{39}Ar$ ages are independent of the P–T history of the grain prior to reaching the T_C. However empirical studies have demonstrated that the temperature history, and more specifically the residence time, metamorphic P–T conditions, the temperature–time path geometry, pressure conditions and grain size, can exert major influence on the $^{40}Ar/^{39}Ar$ ages obtained (Ganguly and Tirone, 1999; Lister and Baldwin, 1996; Viete et al., 2011; Warren et al., 2012a). For example, a grain can yield a date that is older than the time at which the rock reached peak temperature conditions if it grew along the prograde path, and/or contained inherited or excess Ar, and/or only experienced high temperatures (defined as >350 °C by Lister and Baldwin, 1996) for transient (<5 Ma) periods of time.

Ti concentration in both micas varies notably from lowest to highest structural levels (0.03–0.1 pfu and 0.18–0.3 pfu respectively). The significant increase in the Ti concentration, and thus by inference, temperature, occurs around the staurolite isograd, after sample 16, which matches similar findings in the Barrovian metamorphic sequence in Scotland (Viete et al., 2011). The shift in Ti content also coincides with an increased duration of the metamorphic cycle, recorded by U–Pb accessory phase dates and a narrowing of the difference between $^{40}Ar/^{39}Ar$ white mica and biotite sgf dates. This reinforces the previous observations that both the duration of metamorphism and the temperatures reached by samples are critical factors affecting the loss of Ar from mica.

The sgf data show that the widest spread in $^{40}Ar/^{39}Ar$ dates is obtained from samples at structurally lower levels. These mid-temperature range samples (16–17; garnet–staurolite grade) reached temperatures of ~580 °C and display a single monazite age population (Mottram et al., 2014b), suggesting a timescale of <1 Ma for the high-T part of the metamorphic cycle. These samples yield an ~5 Ma spread of sgf $^{40}Ar/^{39}Ar$ dates in white mica and >10 Ma in biotite (Figs. 6–8; Table 3). The biotite in particular, provides unreasonably old crystallisation or cooling ages when compared to the temporal evolution of the wider Himalaya (~15–11 Ma white mica Ar cooling ages in neighbouring Nepal and Bhutan regions e.g. Godin et al., 2001; Stüwe and Foster, 2001). Diffusion modelling suggests that 0.5 mm white mica grains experiencing conditions of ~550 °C and 0.5 GPa for <1 Ma will retain ~5–20% of their ^{40}Ar in an open system (Warren et al., 2012a; see Supplementary material S6.5 for comparison of grain sizes/pressure conditions). The model results suggest that the observed spread of white mica sgf dates from the lower grade samples may have therefore been caused by the retention of radiogenic and/or inherited ^{40}Ar during the metamorphic cycle.

In contrast, samples from the upper parts of the section (samples 19–22, discussion point 5, Fig. 6), reached temperatures of ~650 °C and yield monazite ages suggesting residence at these conditions from ~21 to 16 Ma (Mottram et al., 2014b). These samples all yield white mica plateau ages of ~13 ± 0.3 Ma, and a relatively small spread in white mica sgf dates of only ~2 Ma. A dispersion of this magnitude would be expected due to diffusive differences caused by grain size variations (Supplementary material S6.2). Biotite grains yield a spread in $^{40}Ar/^{39}Ar$ dates of >4 Ma (between ~13.8 and 9.3 Ma). Inverse isochron plots from biotite step-heating experiments in samples 21 and 22 indicate initial $^{36}Ar/^{40}Ar$ concentrations in excess of atmospheric Ar, suggesting that these grains may have incorporated excess Ar during cooling (Supplementary Figures S4.2.2.8–10). Nevertheless, both the biotite and white mica ages are broadly consistent with other temporal constraints on the cooling evolution of the MCT zone (e.g. Godin et al., 2001; Stüwe and Foster, 2001). Diffusion modelling shows that any white mica grain size between 0.1 and 1 mm held at conditions of >600 °C and >0.5 GPa for >0.5 Ma retain <5% ^{40}Ar in an open system (Warren et al., 2012a). These conditions therefore allow for more efficient diffusion.

The lower structural levels of the inverted metamorphic zone beneath the MCT did not therefore reach sufficiently high temperatures long enough for micas to efficiently degas. These samples are likely to have retained an "Ar memory". In contrast, the higher-grade samples, which experienced longer residence times at higher P–T conditions, experienced more efficient diffusion and the dates may be more realistically interpreted as geologically meaningful $^{40}Ar/^{39}Ar$ cooling ages.

7. Diffusion modelling

In order to understand the exhumation history of the MCT zone in Sikkim, a series of numerical modelling experiments were conducted in order to determine the cooling rate that best fits the empirical data. The modelling approach is not dependent on the assumptions implicit in the Dodson Tc formulation and therefore represents a less circular method for estimating rates of cooling.

Forward modelling of Ar diffusion in white mica was undertaken using the MATLAB™ program DiffArg (Wheeler, 1996), following the method of Warren et al. (2012a). Model results were used to determine the best-fit cooling history of samples given their known high temperature history. Models were run from starting temperatures of 550 °C, 600 °C, and 650 °C (the range of temperatures experienced by the rocks across the MCT zone), and at cooling rates in the range 30–80 °C Ma^{-1}, over a time period of 20 Ma. The following parameters were used: a linear cooling rate, a constant pressure of 0.8 GPa (models were also run at 0.4 GPa, shown in the Supplementary material S6.3), the white mica diffusion parameters of Harrison et al. (2009), a Crank–Nicholson solver for the time integration with a time-step of 10 (Wheeler, 1996), a cylindrical diffusion geometry (after Hames

and Bowring, 1994), and 0.5–1 mm diameter grain sizes. Numerical accuracy of the calculations was maximised by running three models at three different mesh sizes and then regressing the bulk ages to the zero mesh size intercept (Warren et al., 2012a). Results are presented in Fig. 10 and in Supplementary material S6.

7.1. Model uncertainties

The diffusion model input parameters have associated uncertainties, the largest of which is the uncertainty in the activation energies. This uncertainty creates a systematic error, which can shift the modelled ages by up to ~±4 Ma depending on the modelled cooling rate (Warren et al., 2012b).

All models were calculated assuming linear cooling from the starting temperatures. However, as the samples were exhumed in a thrust zone, it is likely that their actual cooling history was non-linear. In this dynamic environment hot rocks were steadily thrust over rocks in the relatively colder footwall. Cooling rates may therefore have increased through time as the rocks were progressively exhumed and gradually juxtaposed next to cooler material. A faster initial cooling rate would have the effect of reducing the time gap between the U–Pb and Ar ages. The cooling rates estimated here are therefore minima.

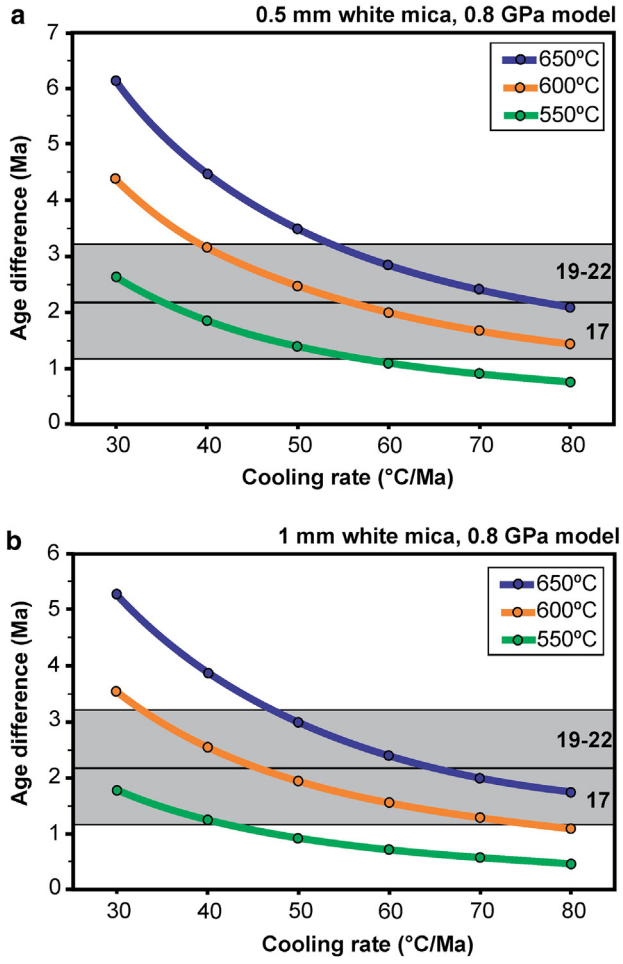

Fig. 10. Summary of Diffarg white mica diffusion model results. Models were run for (a) 0.5 mm and (b) 1 mm grain diameter, and start temperatures of 550 °C, 600 °C and 650 °C and were run at a variety of linear cooling rates from 30 to 80 °C Ma^{-1}, shown on the *x*-axis. The age difference between the age at peak temperature and the model bulk Ar age is shown on the *y*-axis (Table 2). Grey boxes represent the average age difference between U–Pb zircon or monazite ages (age at peak temperature) and the $^{40}Ar/^{39}Ar$ single-grain fusion or step-heating plateau "cooling ages" for each sample set (samples 17/19–22).

The majority of models in this study were run at pressure conditions of 0.8 GPa, following the pseudosection modelling approach of Mottram et al. (2014b). A subset of models were run at a pressure of 0.4 GPa to assess the possibility that micas formed under lower pressure conditions (i.e. Gaidies et al., 2015; phengite barometry in this study). The difference in pressure resulted in a 0.2–0.4 Ma bulk age difference, which is within the range of the analytical measurement uncertainties, and within the uncertainty of the linear regression of the experimental diffusion data (Harrison et al., 2009; Supplementary material S6.3). The results are therefore relatively insensitive to the model pressure, especially when compared to the uncertainties in the diffusion parameters. Likewise, modelling the Ar diffusion in micas as spheres (cf. Harrison et al., 2009) rather than as cylinders (cf. Hames and Bowring, 1994) changes the resulting model ages by <10% (cf. Huber et al., 2011; Supplementary material S6.4).

Grains of ~0.5–1 mm diameter were selected for both $^{40}Ar/^{39}Ar$ single-grain and step-heating experiments, models were therefore based on diffusion radii of 0.25 mm and 0.5 mm. As grains picked for analysis could have represented broken parts of larger crystals, there remains some uncertainty regarding the exact size of the original grains. A few subsidiary models were run using differing grain sizes (0.25–2 mm diameter) to determine the sensitivity of the bulk cooling age to grain size (see data in Supplementary material S6). A difference of 0.25 mm diameter produces a theoretical 1–2 Ma age dispersion. The difference in grain size may therefore explain why different samples (with disparate grain size populations) yield differing spreads in age. However the >5 Ma dispersion of white mica $^{40}Ar/^{39}Ar$ dates obtained from the lower-grade samples cannot be explained entirely by grain size variation, possible alternative causes include unresolvable contamination by extraneous Ar, or influence from inherited ages.

7.2. Modelling results and discussion

Plots of age difference between starting time and model Ar age vs. cooling rate were produced for the three modelled starting temperatures (550 °C, 600 °C and 650 °C) and each grain size (0.5 and 1 mm diameter; Fig. 10). Larger age differences, of up to ~6 Ma, were obtained for slower cooling rates, hotter starting temperatures and smaller grain sizes.

The time difference between the peak metamorphic age and cooling was determined from $^{40}Ar/^{39}Ar$ dates and U–Pb data presented in Fig. 6 and Table 3. The youngest monazite and zircon ages were taken to represent the timing at which cooling initiated (after Mottram et al., 2014b; 2015). The white mica plateau ages from samples 19–22, and the youngest ages in lowest-grade samples (samples 16–17) were taken to represent the cooling ages.

At structurally higher levels, white mica yields younger ages than monazite and zircon, a pattern which should be expected from the relative closure temperatures of zircon at ~900 °C (Cherniak and Watson, 2001), monazite at ~750 °C (Spear and Parrish, 1996), and white mica at ~470 °C (Harrison et al., 2009). At lower metamorphic grades, the U–Pb and $^{40}Ar/^{39}Ar$ ages largely overlap, however the youngest white mica sgf dates (samples 16–17) are ~1.7 Ma younger than the peak metamorphic monazite ages (Table 3). The difference between U–Pb and $^{40}Ar/^{39}Ar$ ages for the higher-grade samples (samples 19–22), ranges between 2.6 and 2.9 Ma (Table 3). All samples are consistent with grain-size-dependent cooling rates between 50 °C Ma^{-1} and 80 °C Ma^{-1} (Fig. 10).

8. Geological implications

8.1. Exhumation of the MCT zone in the Sikkim Himalaya

In the Sikkim Himalaya, metamorphism within the MCT zone was caused by the thrusting of hotter (GHS) material over colder (LHS) material in a pervasive ductile shear zone (i.e. Le Fort, 1975). Deformation

penetrated down from the original thrust surface, through the thrust zone, progressively underplating material from the (LHS) footwall into the (GHS) hanging wall (Larson et al., 2013; Mottram et al., 2014b). The rocks at different levels within the shear zone therefore preserve slightly different thermal histories; rocks at the top of the shear zone experienced higher grades of metamorphism for more prolonged periods and slightly earlier than rocks at the base (Mottram et al., 2014b). This diachroneity could have caused micas to crystallise and recrystallise at different times through the section. However the inverse age relationship between mica and monazite ages (Fig. 6; mica dates young up-section, whilst monazite ages decrease in spread down section; see also Anczkiewicz et al., 2014; Mottram et al., 2014b), suggests that mica dates are unlikely to represent crystallisation ages across the entire metamorphic sequence. The rocks at the structurally highest levels of the inverted metamorphic zone are here considered to yield the most informative $^{40}Ar/^{39}Ar$ cooling ages.

Cooling of the MCT zone was initiated by tectonic movement migrating from the MCT to the structurally lower Ramgarh thrust (RT) and Lesser Himalayan Duplex (LHD) during the mid-late Miocene (Bhattacharyya and Mitra, 2009). The formation of the LHD, coupled with erosion at the surface, caused exhumation, uplift and eventual exposure of the MCT rocks. Our cooling ages provide some of the first timing constraints on the formation of the LHD in the Sikkim Himalaya.

8.2. Comparisons along the Himalaya

The cooling data from the Sikkim Himalaya can be compared with other samples along strike to understand how the rocks in the immediate footwall of the MCT exhumed along the orogen. White mica $^{40}Ar/^{39}Ar$ plateau ages of c.13 Ma from samples 19–22 are consistent with cooling ages of c. 11–14 Ma nearby in the Bhutan Himalaya (McQuarrie et al., 2014; Stüwe and Foster, 2001). In the central Himalaya, cooling ages from the MCT zone range from ~15.5 to 2 Ma (Arita et al., 1997; Copeland et al., 1991; Godin et al., 2001; Hubbard and Harrison, 1989; Macfarlane, 1993; Vannay et al., 2004), suggesting either that exhumation of the MCT zone occurred later in the central part of the orogen, or that differential LHD formation and erosion along strike exposed different structural levels of the fault (e.g. Mottram et al., 2014b).

8.3. Coeval movement on structures?

The South Tibetan Detachment (STD) is a normal fault which forms the northern boundary of the GHS. The (coeval) movement of the STD and MCT is of key importance for models of extrusion of the GHS in all Himalayan tectonic models (see reviews of Godin et al., 2006; Harris, 2007; Hodges, 2000). Overall the white mica cooling ages obtained for the leading-edge of the MCT in the Sikkim Himalaya overlap within error with the ~13 Ma cooling age for the STD in the north of the Sikkim Himalaya (Kellett et al., 2013), suggesting that exhumation and cooling occurred simultaneously on both the MCT and STD in the region. An $^{40}Ar/^{39}Ar$ cooling age of c.13 Ma have been obtained for the STD throughout the eastern Himalaya (Kellett and Godin, 2009; Kellett et al., 2013; Leloup et al., 2010), suggesting that the STD was simultaneously cooling and exhuming at various along-strike locations, from eastern Nepal into Bhutan.

8.4. Cooling rates

It has been estimated that cooling rates in the GHS were rapid during the early to mid-Miocene, with rates varying between 10 and 60 °C Ma^{-1} in the GHS of NW India (Vannay et al., 2004), 50 °C Ma^{-1} in the GHS of Nepal (Godin et al., 2001), and ~150–200 °C Ma^{-1} in the Sikkim and Bhutan Himalaya (Kellett et al., 2013; McQuarrie et al., 2014). Differing cooling rates obtained along strike probably reflect deformation around large-scale structures that accommodated exhumation. After the initial rapid cooling, it has been suggested that cooling rates slowed during the Miocene–Pliocene (McQuarrie et al., 2014; Vannay and Grasemann, 2001), decreasing to 20 °C Ma^{-1} in NW India (Vannay et al., 2004), and 7 °C Ma^{-1} in the Sikkim Himalaya (Kellett et al., 2013). Our estimated cooling rate of ~50–80 °C Ma^{-1}, between c. 16 and 13 Ma, fits with previous suggestions for mid-Miocene cooling rates across the GHS of ~50 °C Ma^{-1}. It appears that the mid-Miocene was a time of rapid thrusting, extrusion and cooling of the rocks within the MCT zone, with possible simultaneous cooling on both the STD and MCT in the Sikkim Himalaya, perhaps initiated by deformation migrating towards the hinterland.

9. Conclusions

$^{40}Ar/^{39}Ar$ data collected from a detailed transect through an inverted metamorphic sequence reveals important insights into Ar behaviour in pelitic lithologies during a Barrovian metamorphic cycle over a range of temperatures. Single-grain fusion and step-heating data from Sikkim Himalayan samples reveal that both white mica and biotite age populations become younger, less dispersed and preserve a narrower age difference between the two micas as temperature increases. The differences in the $^{40}Ar/^{39}Ar$ dates across the MCT section appear to be caused not by differential cooling histories, but rather by differences in the efficiency of Ar removal. These differences were caused by a combination of diffusion (in)efficiency (related to temperature and time), the influence of excess Ar in biotite and differences in availability of fluid to remove any grain-boundary-hosted Ar.

The rocks that experienced a more prolonged period of metamorphism at higher temperatures, yield the most geologically reasonable cooling ages of ~13 Ma. At these P–T conditions, efficient diffusion, allows for minimal retention of ^{40}Ar even during short orogenic cycles (<5 Ma). Our data therefore provide empirical evidence to support modelling data, demonstrating that temperatures maintained at >600 °C over a period of ~5 Ma are needed for mica to record diffusive cooling ages. This critical temperature is considerably higher than the documented closure temperature for white mica. Our work therefore highlights the need to determine the full P–T history and efficiency of Ar diffusion in order to understand whether an $^{40}Ar/^{39}Ar$ "date" constrains the timing of cooling.

Diffusion modelling results suggest a best-fit cooling rate of ~50–80 °C Ma^{-1} for the highest-grade samples. Our data reveal that despite being buried and metamorphosed at different times throughout the MCT zone section, samples were simultaneously and rapidly cooled during exhumation due to the formation of the underlying Lesser Himalayan Duplex during the mid-Miocene. Cooling ages from the Sikkim Himalaya also overlap with ages from the South Tibetan Detachment in Sikkim, suggesting coeval exhumation along the MCT and STD rocks at ~13 Ma.

Supplementary data to this article can be found online at http://dx.doi.org/10.1016/j.lithos.2015.08.018.

Acknowledgements

This study was funded by a NERC PhD studentship awarded to C.M (NE/1528018/1), a NERC Advanced Fellowship awarded to C.W (NE/HO16279/1) and a Royal Society International Joint Project grant (IJP 2008/R3) awarded to Nigel Harris, Saibal Gupta and Tom Argles. U–Pb analytical work was funded by a NERC facility grant awarded to N.H and C.M (IP-1129-0511). We thank Michelle Higgins and Kay Green for help with sample preparation; Sarah Sherlock, James Schwanethal (who developed the ArMaDiLo software) and James Malley for technical help in the Ar lab; Andy Tindle for technical support with EPMA; Vanessa Pashley and Nick Roberts for help with zircon analyses; Daniele Regis and Tom Argles with help and discussion regarding P–T work; Chris McDonald for help with DiffArg diffusion modelling; and Saibal Gupta, Souvik Mitra, Lucy Greenwood, Tenpa Chophel and Kesang

Sherpa for help in the field. Many thanks to Susanne Schneider, Daniel Viete and an anonymous reviewer for comments that significantly improved the manuscript.

References

Anczkiewicz, R., Chakraborty, S., Dasgupta, S., Mukhopadhyay, D., Kołtonik, K., 2014. Timing, duration and inversion of prograde Barrovian metamorphism constrained by high resolution Lu–Hf garnet dating: a case study from the Sikkim Himalaya, NE India. Earth and Planetary Science Letters 407, 70–81.

Arita, K., Dallmeyer, R.D., Takasu, A., 1997. Tectonothermal evolution of the Lesser Himalaya, Nepal: constraints from 40Ar/39Ar ages from the Kathmandu Nappe. õlsland Arc 6, 372–385.

Arnaud, N., Kelley, S.P., 1995. Evidence for excess argon during high pressure metamorphism in the Dora Maira Massif (western Alps, Italy), using an ultra-violet laser ablation microprobe 40Ar–39Ar technique. Contributions to Mineralogy and Petrology 121, 1–11.

Barrow, G., 1893. On an intrusion of muscovite–biotite gneiss in the south-eastern Highlands of Scotland, and its accompanying metamorphism. Quarterly Journal of the Geological Society 49 (1–4), 330–358.

Baxter, E.F., DePaolo, D.J., Renne, P.R., 2002. Spatially correlated anomalous 40Ar/39Ar "age" variations in biotites about a lithologic contact near Simplon Pass, Switzerland: a mechanistic explanation for excess Ar. Geochimica Et Cosmochimica Acta 66, 1067–1083.

Beltrando, M., Lister, G.S., Forster, M., Dunlap, W.J., Fraser, G., Hermann, J., 2009. Dating microstructures by the 40Ar/39Ar step-heating technique: deformation–pressure–temperature–time history of the Penninic Units of the Western Alps. Lithos 113, 801–819.

Bhattacharya, A., Mohanty, L., Maji, A., Sen, S., Raith, M., 1992. Non-ideal mixing in the phlogopite–annite binary: constraints from experimental data on Mg–Fe partitioning and a reformulation of the biotite–garnet geothermometer. Contributions to Mineralogy and Petrology 111, 87–93.

Bhattacharyya, K., Mitra, G., 2009. A new kinematic evolutionary model for the growth of a duplex—an example from the Rangit duplex, Sikkim Himalaya, India. Gondwana Research 16, 697–715.

Brewer, M.S., 1969. Excess radiogenic argon in metamorphic micas from the eastern ALPS, Austria. Earth and Planetary Science Letters 6 (5), 321–331.

Cherniak, D., Watson, E., 2001. Pb diffusion in zircon. Chemical Geology 172, 5–24.

Chopin, C., Maluski, H., 1980. 40Ar–39Ar dating of high pressure metamorphic micas from the Gran Paradiso area (Western Alps): evidence against the blocking temperature concept. Contributions to Mineralogy and Petrology 74, 109–122.

Copeland, P., Harrison, T.M., Hodges, K.V., Maruéjol, P., Le Fort, P., Pecher, A., 1991. An early Pliocene thermal disturbance of the Main Central Thrust, central Nepal: implications for Himalayan tectonics. Journal of Geophysical Research: Solid Earth (1978–2012) 96, 8475–8500.

Cosca, M., Stunitz, H., Bourgeix, A.L., Lee, J.P., 2011. 40Ar* loss in experimentally deformed muscovite and biotite with implications for 40Ar/39Ar geochronology of naturally deformed rocks. Geochimica et Cosmochimica Acta 75 (24), 7759–7778.

Dahl, P.S., 1996. The effects of composition on retentivity of argon and oxygen in hornblende and related amphiboles: a field-tested empirical model. Geochimica et Cosmochimica Acta 60 (19), 3687–3700.

Dasgupta, S., Ganguly, J., Neogi, S., 2004. Inverted metamorphic sequence in the Sikkim Himalayas: crystallization history, P–T gradient and implications. Journal of Metamorphic Geology 22, 395–412.

Dasgupta, S., Chakraborty, S., Neogi, S., 2009. Petrology of an inverted Barrovian Sequence of metapelites in Sikkim Himalaya, India: constraints on the tectonics of inversion. American Journal of Science 309, 43–84.

Dempster, T., 1992. Zoning and recrystallization of phengitic micas: implications for metamorphic equilibration. Contributions to Mineralogy and Petrology 109, 526–537.

Di Vincenzo, G., Palmeri, R., 2001. An 40Ar–39Ar investigation of high-pressure metamorphism and the retrogressive history of mafic eclogites from the Lanterman Range (Antarctica): evidence against a simple temperature control on argon transport in amphibole. Contributions to Mineralogy and Petrology 141, 15–35.

Di Vincenzo, G., Ghiribelli, B., Giorgetti, G., Palmeri, R., 2001. Evidence of a close link between petrology and isotope records: constraints from SEM, EMP, TEM and in situ 40Ar–39Ar laser analyses on multiple generations of white micas (Lanterman Range, Antarctica). Earth and Planetary Science Letters 192, 389–405.

Dodson, M.H., 1973. Closure temperature in cooling geochronological and petrological systems. Contributions to Mineralogy and Petrology 40, 259–274.

Dubey, C.S., Catlos, E.J., Sharma, B.K., 2005. Modelling of P–T–t paths constrained by mineral chemistry and monazite dating of metapelites in relationship to MCT activity in Sikkim Eastern Himalayas. In: Thomas, H. (Ed.), Metamorphism and Crustal Evolution. Atlantic publishers, New Delhi, pp. 250–282.

Dunlap, W.J., 1997. Neocrystallization or cooling? 40Ar/39Ar ages of white micas from low-grade mylonites. Chemical Geology 143 (3), 181–203.

Dunlap, W.J., Teyssier, C., McDougall, I., Baldwin, S., 1991. Ages of deformation from K/Ar and 40Ar/39Ar dating of white micas. Geology 19 (12), 1213–1216.

Foland, K., 1979. Limited mobility of argon in a metamorphic terrain. Geochimica Et Cosmochimica Acta 43, 793–801.

Gaidies, F., Petley-Ragan, A., Chakraborty, S., Dasgupta, S., Jones, P., 2015. Constraining the conditions of Barrovian metamorphism in Sikkim, India: P–T–t paths of garnet crystallization in the Lesser Himalayan Belt. Journal of Metamorphic Geology 33 (1), 23–44.

Ganguly, J., Tirone, M., 1999. Diffusion closure temperature and age of a mineral with arbitrary extent of diffusion: theoretical formulation and applications. Earth and Planetary Science Letters 170 (1–2), 131–140.

Gasser, D., Bruand, E., Rubatto, D., Stüwe, K., 2012. The behaviour of monazite from greenschist facies phyllites to anatectic gneisses: an example from the Chugach Metamorphic Complex, southern Alaska. Lithos 134, 108–122.

Godin, L., Parrish, R.R., Brown, R.L., Hodges, K.V., 2001. Crustal thickening leading to exhumation of the Himalayan metamorphic core of central Nepal: insight from U–Pb geochronology and 40Ar/39Ar thermochronology. Tectonics 20, 729–747.

Godin, L., Grujic, D., Law, R., Searle, M., 2006. Channel flow, ductile extrusion and exhumation in continental collision zones: an introduction. Geological Society, London, Special Publications 268, 1–23.

Halama, R., Konrad-Schmolke, M., Sudo, M., Marschall, H.R., Wiedenbeck, M., 2014. Effects of fluid–rock interaction on 40Ar/39Ar geochronology in high-pressure rocks (Sesia-Lanzo Zone, Western Alps). Geochimica Et Cosmochimica Acta 126, 475–494.

Hames, W.E., Bowring, S.A., 1994. An empirical evaluation of the argon diffusion geometry in muscovite. Earth and Planetary Science Letters 124 (1), 161–169.

Hames, W.E., Cheney, J., 1997. On the loss of 40Ar* from muscovite during polymetamorphism. Geochimica Et Cosmochimica Acta 61, 3863–3872.

Hammerschmidt, K., Frank, E., 1991. Relics of high-pressure metamorphism in the Lepontine Alps (Switzerland)—40Ar/39Ar and microprobe analyses on white K-micas. Schweizerische Mineralogische und Petrographische Mitteilungen 71, 261–274.

Harris, N., 2007. Channel flow and the Himalayan–Tibetan orogen: a critical review. Journal of the Geological Society 164, 511–523.

Harrison, T.M., Duncan, I., McDougall, I., 1985. Diffusion of 40Ar in biotite: temperature, pressure and compositional effects. Geochimica Et Cosmochimica Acta 49, 2461–2468.

Harrison, T.M., Célérier, J., Aikman, A.B., Hermann, J., Heizler, M.T., 2009. Diffusion of 40Ar in muscovite. Geochimica Et Cosmochimica Acta 73, 1039–1051.

Henry, D.J., Guidotti, C.V., Thomson, J.A., 2005. The Ti-saturation surface for low-to-medium pressure metapelitic biotites: implications for geothermometry and Ti-substitution mechanisms. American Mineralogist 90, 316–328.

Hodges, K.V., 2000. Tectonics of the Himalaya and southern Tibet from two perspectives. Geological Society of America Bulletin 112, 324–350.

Hubbard, M.S., Harrison, T.M., 1989. 40Ar/39Ar age constraints on deformation and metamorphism in the Main Central Thrust zone and Tibetan Slab, eastern Nepal Himalaya. Tectonics 8, 865–880.

Huber, C., Cassata, W.S., Renne, P.R., 2011. A lattice Boltzmann model for noble gas diffusion in solids: the importance of domain shape and diffusive anisotropy and implications for thermochronometry. Geochimica et Cosmochimica Acta 75 (8), 2170–2186.

Itaya, T., Hyodo, H., Tsujimori, T., Wallis, S., Aoya, M., Kawakami, T., Gouzu, C., 2009. Regional-scale excess Ar wave in a Barrovian type metamorphic belt, eastern Tibetan Plateau. Island Arc 18, 293–305.

Jackson, C.R., Parman, S.W., Kelley, S.P., Cooper, R.F., 2013. Noble gas transport into the mantle facilitated by high solubility in amphibole. Nature Geoscience 6, 562–565.

Janots, E., Brunet, F., Goffé, B., Poinssot, C., Burchard, M., Cemič, L., 2007. Thermochemistry of monazite–(La) and dissakisite–(La): implications for monazite and allanite stability in metapelites. Contributions to Mineralogy and Petrology 154, 1–14.

Janots, E., Engi, M., Berger, A., Allaz, J., Schwarz, J.O., Spandler, C., 2008. Prograde metamorphic sequence of REE minerals in pelitic rocks of the Central Alps: implications for allanite–monazite–xenotime phase relations from 250 to 610 C. Journal of Metamorphic Geology 26, 509–526.

Kellett, D.A., Godin, L., 2009. Pre-Miocene deformation of the Himalayan superstructure, Hidden Valley, central Nepal. Journal of the Geological Society 166, 261–275.

Kellett, D.A., Grujic, D., Coutand, I., Cottle, J., Mukul, M., 2013. The South Tibetan detachment system facilitates ultra rapid cooling of granulite–facies rocks in Sikkim Himalaya. Tectonics.

Kelley, S., 2002. Excess argon in K–Ar and Ar–Ar geochronology. Chemical Geology 188, 1–22.

Kirschner, D.L., Cosca, M.A., Masson, H., Hunziker, J.C., 1996. Staircase 40/Ar39Ar spectra of fine-grained white mica: timing and duration of deformation and empirical constraints on argon diffusion. Geology 24 (8), 747–750.

Kramar, N., Cosca, M.A., Hunziker, J.C., 2001. Heterogeneous 40Ar* distributions in naturally deformed muscovite: in situ UV-laser ablation evidence for microstructurally controlled intragrain diffusion. Earth and Planetary Science Letters 192 (3), 377–388.

Krenn, E., Finger, F., 2007. Formation of monazite and rhabdophane at the expense of allanite during Alpine low temperature retrogression of metapelitic basement rocks from Crete, Greece: microprobe data and geochronological implications. Lithos 95, 130–147.

Kula, J., Spell, T.L., Zanetti, K.A., 2010. 40Ar/39Ar analyses of artificially mixed micas and the treatment of complex age spectra from samples with multiple mica populations. Chemical Geology 275, 67–77.

Larson, K.P., Gervais, F., Kellett, D.A., 2013. A P–T–t–D discontinuity in east-central Nepal: Implications for the evolution of the Himalayan mid-crust. Lithos 179, 275–292.

Le Fort, P., 1975. Himalayas: the collided range. Present knowledge of the continental arc. American Journal of Science 275 (1), 44.

Lee, Jee-Yon, Marti, Kurt, Severinghaus, Jeffrey P., Kawamura, Kenji, Yoo, Hee-Soo, Lee, Jin Bok, Kim, Jin Seog, 2006. A redetermination of the isotopic abundances of atmospheric Ar. Geochimica et Cosmochimica Acta 70, 4507–4512.

Leloup, P., Mahéo, G., Arnaud, N., Kali, E., Boutonnet, E., Liu, D., Xiaohan, L., Haibing, L., 2010. The South Tibet detachment shear zone in the Dinggye area: time constraints on extrusion models of the Himalayas. Earth and Planetary Science Letters 292, 1–16.

Lister, G.S., Baldwin, S.L., 1996. Modelling the effect of arbitrary PTt histories on argon diffusion in minerals using the MacArgon program for the Apple Macintosh. Tectonophysics 253, 83–109.
Ludwig, K.R., 2003. A Geochronological Toolkit for Microsoft Excel. Berkeley Geochronology Center, Special, Publication. 4 p. 71.
Macfarlane, A., 1993. Chronology of tectonic events in the crystalline core of the Himalaya, Langtang National Park, central Nepal. Tectonics 12, 1004–1025.
Massonne, H.J., Schreyer, W., 1987. Phengite geobarometry based on the limiting assemblage with K-feldspar, phlogopite, and quartz. Contributions to Mineralogy and Petrology 96 (2), 212–224.
McDougall, I., Harrison, T.M., 1999. Geochronology and Thermochronology by the 40Ar/39Ar Method. Oxford University Press.
McQuarrie, N., Tobgay, T., Long, S.P., Reiners, P.W., Cosca, M.A., 2014. Variable exhumation rates and variable displacement rates: documenting recent slowing of Himalayan shortening in western Bhutan. Earth and Planetary Science Letters 386, 161–174.
Min, K., Mundil, R., Renne, P.R., Ludwig, K.R., 2000. A test for systematic errors in 40Ar/39Ar geochronology through comparison with U/Pb analysis of a 1.1-Ga rhyolite. Geochimica Et Cosmochimica Acta 64 (1), 73–98.
Mottram, C.M., Argles, T., Parrish, R., Harris, N., Horstwood, M., Gupta, S., 2014a. Tectonic interleaving along the Main Central Thrust, Sikkim Himalaya. Journal of the Geological Society 171, 255–268.
Mottram, C.M., Warren, C.J., Regis, D., Roberts, N.M.W., Harris, N., Argles, T., Parrish, R., 2014b. Developing an inverted Barrovian sequence; insights from monazite petrochronology. Earth and Planetary Science Letters 403, 418–431.
Mottram, C.M., Parrish, R.R., Regis, D., Warren, C.J., Argles, T.W., Harris, N.B.W., Roberts, N.M.W., 2015. Using U–Th–Pb petrochronology to determine rates of ductile thrusting: time windows into the Main Central Thrust, Sikkim Himalaya. Tectonics 34. http://dx.doi.org/10.1002/2014TC003743.
Najman, Y., Appel, E., Boudagher-Fadel, M., Bown, P., Carter, A., Garzanti, E., ... Vezzoli, G., 2010. Timing of India-Asia collision: Geological, biostratigraphic, and palaeomagnetic constraints. Journal of Geophysical Research: Solid Earth (1978–2012), 115(B12).
Oliver, G.J.H., Chen, F., Buchwaldt, R., Hegner, E., 2000. Fast tectonometamorphism and exhumation in the type area of the Barrovian and Buchan zones. Geology 28 (5), 459–462.
Powell, R., Holland, T.J.B., 1988. An internally consistent dataset with uncertainties and correlations. 3. Applications to geobarometry, worked examples and a computer program. Journal of Metamorphic Geology 6, 173–204.
Rasmussen, B., Muhling, J.R., 2009. Reactions destroying detrital monazite in greenschist-facies sandstones from the Witwatersrand basin, South Africa. Chemical Geology 264, 311–327.
Reddy, S.M., Potts, G.J., Kelley, S.P., 2001. 40Ar/39Ar ages in deformed potassium feldspar: evidence of microstructural control on Ar isotope systematics. Contributions to Mineralogy and Petrology 141 (2), 186–200.
Renne, P.R., Mundil, R., Balco, G., Min, K., Ludwig, K.R., 2010. Joint determination of 40K decay constants and 40Ar*/40K for the Fish Canyon sanidine standard, and improved accuracy for 40Ar/39Ar geochronology. Geochimica Et Cosmochimica Acta 74 (18), 5349.
Roddick, J., Cliff, R., Rex, D., 1980. The evolution of excess argon in alpine biotites—A 40Ar/39Ar analysis. Earth and Planetary Science Letters 48, 185–208.
Ruffet, G., Féraud, G., Balèvre, M., Kiénast, J.-R., 1995. Plateau ages and excess argon in phengites: an 40Ar/39Ar laser probe study of Alpine micas (Sesia Zone, Western Alps, northern Italy). Chemical Geology 121, 327–343.
Smith, H.A., Barreiro, B., 1990. Monazite U–Pb dating of staurolite grade metamorphism in pelitic schists. Contributions to Mineralogy and Petrology 105, 602–615.
Smye, A.J., Warren, C.J., Bickle, M.J., 2013. The signature of devolatisation: extraneous 40Ar systematics in high-pressure metamorphic rocks. Geochimica Et Cosmochimica Acta 113, 94–112.
Spear, F.S., Parrish, R.R., 1996. Petrology and cooling rates of the Valhalla complex, British Columbia, Canada. Journal of Petrology 37, 733–765.
Stüwe, K., Foster, D., 2001. 40Ar/39Ar, pressure, temperature and fission track constraints on the age and nature of metamorphism around the main central thrust in the eastern Bhutan Himalaya. Journal of Asian Earth Sciences 19, 85–95.
Vannay, J.-C., Grasemann, B., 2001. Himalayan inverted metamorphism and syn-convergence extension as a consequence of a general shear extrusion. Geological Magazine 138, 253–276.
Vannay, J.C., Grasemann, B., Rahn, M., Frank, W., Carter, A., Baudraz, V., Cosca, M., 2004. Miocene to Holocene exhumation of metamorphic crustal wedges in the NW Himalaya: evidence for tectonic extrusion coupled to fluvial erosion. Tectonics 23.
Viete, D.R., Forster, M.A., Lister, G.S., 2011. The nature and origin of the Barrovian metamorphism, Scotland: 40Ar/39Ar apparent age patterns and the duration of metamorphism in the biotite zone. Journal of the Geological Society 168, 133–146.
Warren, C.J., Hanke, F., Kelley, S.P., 2012a. When can muscovite 40Ar/39Ar dating constrain the timing of metamorphic exhumation? Chemical Geology 291, 79–86.
Warren, C.J., Kelley, S.P., Sherlock, S.C., McDonald, C.S., 2012b. Metamorphic rocks seek meaningful cooling rate: interpreting 40Ar/39Ar ages in an exhumed ultra-high pressure terrane. Lithos 155, 30–48.
Warren, C.J., Singh, A.K., Roberts, N.M.W., Regis, D., Halton, A.M., Singh, R.B., 2014. Timing and conditions of peak metamorphism and cooling across the Zimithang Thrust, Arunachal Pradesh, India. Lithos 200–201, 94–110. http://dx.doi.org/10.1016/j.lithos.2014.04.005.
Wartho, J.-A., Kelley, S.P., Elphick, S.C., 2013. Advances in 40Ar/39Ar dating: from archaeology to planetary sciences, Ar diffusion and solubility measurements in plagioclases using the ultra-violet laser depth-profiling technique. Geological Society, London, Special Publications 378, 137–154.
Wheeler, J., 1996. DIFFARG: a program for simulating argon diffusion profiles in minerals. Computers & Geosciences 22, 919–929.
Whitney, D., Evans, B., 2010. Abbreviations for names of rock-forming minerals. American mineralogist 95 (1), 185.